REVIEW ARTICLE | MAY 23 2022

Ultrafast photo-induced processes in complex environments: The role of accuracy in excited-state energy potentials and initial conditions

Alessio Petrone ; Fulvio Perrella ; Federico Coppola ; Luigi Crisci ; Greta Donati ; Paola Cimino ; Nadia Rega

Chem. Phys. Rev. 3, 021307 (2022)
https://doi.org/10.1063/5.0085512

Chemical Physics Reviews REVIEW scitation.org/journal/cpr

Ultrafast photo-induced processes in complex environments: The role of accuracy in excited-state energy potentials and initial conditions

Cite as: Chem. Phys. Rev. **3**, 021307 (2022); doi: 10.1063/5.0085512
Submitted: 17 January 2022 · Accepted: 19 April 2022 ·
Published Online: 23 May 2022

Alessio Petrone,[1,2,a] Fulvio Perrella,[1,b] Federico Coppola,[1,b] Luigi Crisci,[1] Greta Donati,[1,c] Paola Cimino,[3] and Nadia Rega[1,2,4,a]

AFFILIATIONS

[1]Department of Chemical Sciences, University of Napoli Federico II, Complesso Universitario di M.S. Angelo, via Cintia 21, I-80126 Napoli, Italy
[2]Scuola Superiore Meridionale, Largo San Marcellino 10, I-80138 Napoli, Italy
[3]Department of Pharmaceutical Sciences, University of Salerno, via Ponte don Melillo, I-84084 Fisciano, SA, Italy
[4]CRIB, Centro Interdipartimentale di Ricerca sui Biomateriali, Piazzale Tecchio 80, I-80125 Napoli, Italy

[a]**Authors to whom correspondence should be addressed:** alessio.petrone@unina.it and nadia.rega@unina.it
[b]**Present address:** Scuola Superiore Meridionale, Largo San Marcellino 10, I-80138 Napoli, Italy.
[c]**Present address:** Department of Pharmacy, University of Napoli Federico II, Via D. Montesano 49, I-80131 Napoli, Italy.

ABSTRACT

Light induces non-equilibrium time evolving molecular phenomena. The computational modeling of photo-induced processes in large systems, embedded in complex environments (i.e., solutions, proteins, materials), demands for a quantum and statistical mechanic treatment to achieve the required accuracy in the description of both the excited-state energy potentials and the choice of the initial conditions for dynamical simulations. On the other hand, the theoretical investigation on the atomistic scale of times and sizes of the ultrafast photo-induced reactivity and non-equilibrium relaxation dynamics right upon excitation requests tailored computational protocols. These methods often exploit hierarchic computation schemes, where a large part of the degrees of freedom are required to be treated explicitly to achieve the right accuracy. Additionally, part of the explicit system needs to be treated at *ab initio* level, where density functional theory, using hybrid functionals, represents a good compromise between accuracy and computational cost, when proton transfers, non-covalent interactions, and hydrogen bond dynamics play important roles. Thus, the modeling strategies presented in this review stress the importance of hierarchical quantum/molecular mechanics with effective non-periodic boundary conditions and efficient phase-sampling schemes to achieve chemical accuracy in ultrafast time-resolved spectroscopy and photo-induced phenomena. These approaches can allow explicit and accurate treatment of molecule/environment interactions, including also the electrostatic and dispersion forces of the bulk. At the same time, the specificities of the different case studies of photo-induced phenomena in solutions and biological environments are highlighted and discussed, with special attention to the computational and modeling challenges.

TABLE OF CONTENTS

I. INTRODUCTION

The comprehension of chemical reactivity and non-equilibrium processes induced by the light requires a dynamical description of the system under study. In this regard, quantum and statistical mechanics define the playgrounds for the theoretical study of such events on the atomistic scale of times (picoseconds) and sizes (picometers).[1–3] Dealing with photo-induced phenomena, an accurate description of the energy potential ruling the system dynamics is demanded, since an electronic density reorganization is always involved. This is usually quite common when chemical reactions, that is, bond breaking and reformation, and environment reorganizations are in play. Since parameterized force fields cannot account for explicit electronic effects, an explicit treatment of electronic degrees of freedom is mandatory. On the other hand, when large systems ($\gtrapprox$1000 atoms) are involved, wavefunction-based methods cannot be pursued given the high computational cost (above all when excited-state properties are computed), although several progresses have been recently achieved using graphical processing units[4] and localization procedures.[5,6] Thus, density functional theory (DFT) becomes the method of election. However, the issue is still open, since DFT and time-dependent (TD-) DFT, this last one required for excited-state quantities, are still computationally demanding methods, and, therefore, not all degrees of freedom can be explicitly accounted for anyway. In the past decades, model Hamiltonians,[7,8] semi-empirical quantum-chemical methods,[9,10] and tight binding potentials[11] have been vastly employed to study excited-state evolution and non-adiabatic phenomena for their reduced computational costs. These approximated methods are very important in kinetic studies, allowing to run thousands of trajectories, indeed. Pioneering works employing non-adiabatic surface hopping dynamics on parameterized potentials have allowed the study of ultrafast photodynamics of photoswitches,[12,13] and the exciton migration in inorganic substrates has also been recently investigated via excited-state *ab initio* molecular dynamics (AIMD).[14,15] The opportunity of direct approaches and the fitting of potential energy surfaces have been compared in a recent publication[16] along with improved algorithms to speed up these computationally demanding simulations.[17]

However, when the excited-state relaxation mechanism is ruled by several weak interactions (i.e., solute–solvent) and by small changes in the electronic density, a more detailed description of the system, with more accurate methods, cannot be avoided. This is a huge challenge for the theoretical study of the interplay between molecules in complex environments (i.e., solutions) and their related non-equilibrium properties (i.e., time-resolved spectroscopic signals). The environment surrounding the system under investigation can highly impact on the spectroscopic properties and photoreactivity of macromolecules in condensed phase, that is, in protic and/or polar solvents.[18–24] This is not a negligible issue, and the modeling of how the solute interacts with the solvent is critical to both understand and tune the properties of a system embedded in complex matrices.[25–27] It is well known in the literature how absorption and emission band shapes and positions are deeply influenced by polarization and electrostatic interactions caused by the surrounding molecules.[28–35] Thus, the theoretical investigation of photo-induced reactivity and optical properties of probe-solvent-specific interactions needs to provide reliable protocols and models to completely include the role and the influence of environments, that is, solvents, proteins, DNA, surfaces, or polymeric matrices in a dynamical way. Hybrid quantum/classical (QM/MM) methods and more, in general, multilayer computational schemes have allowed the structural and dynamics characterization of macromolecular systems, even large biomolecules in complex environments.[36–47] In this regard, QM/MM *ab initio* molecular dynamics (AIMD) of non-periodic systems, for example, liquids and solutions, have vastly employed free energy surfaces (FESs). In addition to the potential energy contribution, calculated taking into account all the explicit interactions of the QM and MM parts, one has to be able also to include the long-range matrix effects, by factoring part of their degrees of freedom into the free energy contributions. Only in this way, it is possible to simultaneously describe both the microsolvation structure and the bulk/matrix effects (i.e., as ensemble averages).[29,31,48] In this context, (AI)MD can be based either on the use of periodic boundary conditions (PBCs), which arise naturally when, for example, the electronic density is described in terms of periodic plane waves,[49] or on the employment of non-periodic (i.e., spherical) boundary conditions (NPBCs).[50–58] Charged species can be directly described by NPBCs, since they can easily combine QM/MM multilayer schemes and DFT codes employing localized Gaussian basis functions. Localized basis functions allow us to compute exact HF exchange with no further computational effort and so the adoption of hybrid density functionals, which can provide more accurate predictions in the computation of activation energies. This is particularly true when hydrogen atom motions are in play, such as in the formation of protonated complex and the dynamics of hydrogen bonds (HBs),[48,58–61] or when is required an accurate treatment of the electronic structure of materials[62–71] along with transient optical properties.[48,72–77] Another main player in achieving accurate potentials is the description of the solvent molecules. It becomes fundamental not only an explicit treatment of their degrees of freedom, via an atomistic description of a significant part of solvent molecules, but also flexible models are required. This is crucial for obtaining a high-level description of solute–solvent time-dependent interactions, in particular hydrogen

bond networks, strongly affecting the accuracy of several system properties, that is, solvent viscosity, mobility of solvation shells (less artificially rigid), and solute–solvent vibrational couplings. Computational scientists have to take into account both an accurate description of active site/solute with the environment/solvent, via the employment of an *ab initio* potential energy surface (PES) including short- and long-range interactions with the bulk solvent or a complex matrix, and a detailed simulation of the thermal equilibrium of all degrees of freedom, via efficient phase-sampling schemes. Thus, in this review we stress the importance of hierarchical quantum/molecular mechanics combined with *ab initio* MD with effective non-periodic boundary conditions and efficient phase-sampling schemes to achieve chemical accuracy in ultrafast time-resolved spectroscopy and photo-induced phenomena.

II. *AB INITIO* POTENTIALS AND PHASE-SPACE SAMPLING: CHALLENGES AND SOLUTIONS FOR NON-EQUILIBRIUM EXCITED-STATE SIMULATIONS

A. Building a reliable free energy surface for a given electronic state

The following summarized combined protocol for building an accurate hybrid DFT-based FES, adopting the hybrid QM/MM scheme—including flexible solvent molecules—and NPBC, has been extensively discussed in Ref. 60. In the past years, such approach has been proven to be accurate and efficient in several studies, where also large macromolecular systems and electronic excitations have been investigated.[48,58,61,73,78–81] A short review is proposed here. An empirical effective free energy term is added to the total energy via an analytic expression. This term includes the energy contributions due to the interactions of the explicit solvent molecules (included in a spherical molecular cluster) and the implicit bulk; such interactions have either a Coulombic or a dispersive, London-like, nature. In this way, the effects of the bulk are explicitly present in terms of effective forces acting on the explicit part, enforcing boundary conditions. We consider a solute–solvent system described at atomistic level (explicit system) confined by a sphere of fixed radius and perturbed by the mean field of the surrounding bulk solvent, which is represented implicitly. We then assume the Born–Oppenheimer approximation for the explicit part, described by the nuclear coordinates $\mathbf{R}$ and by the one-electron density matrix $\mathbf{P}^n$, which refers to the n-th electronic state of interest. The part explicitly described adopts the canonical ensemble, even if the isothermal–isobaric ensemble can be also used.[82] As customary in so-called focused models, we can define the Helmholtz free energy, for a given n-th electronic state and configuration $\mathbf{R}$ of the explicit system in solution, as

$$A^n(\mathbf{R}) = E^n(\mathbf{P}^n, \mathbf{R}) + W^n(\mathbf{P}^n, \mathbf{R}), \tag{1}$$

where $E^n(\mathbf{P}^n, \mathbf{R})$ and $W^n(\mathbf{P}^n, \mathbf{R})$ are the potential and the average solvation energies relative to the n-th electronic state, respectively. We wish to point out that the solvent mean field contribution has a part that explicitly depends on $\mathbf{P}^n$. This means that is tailored on the n-th excited-state response, since the implicit and the explicit parts are able to mutually polarize (and be polarized). $\mathbf{P}^n$ in the two terms in rhs of Eq. (1) can be computed with any *ab initio* method capable to obtain also excited-state properties (for $n \neq 0$). W represents the work required to charge the interactions between the implicit and explicit parts of the system. According to the Ben-Naim description of the solvation process,[83] W can be empirically decomposed as follows:

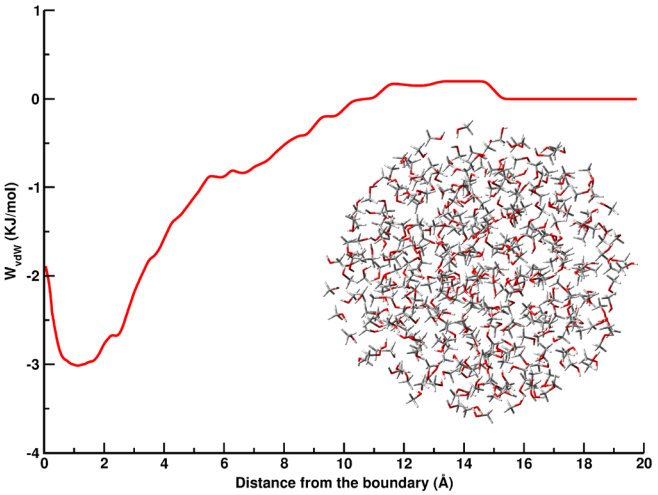

FIG. 1. $W_{disp-rep}$ radial energy potential resulting from the parameterization procedure presented in Refs. 55 and 60 for CH_3OH as function of the distance from the boundary, *r*. The presented radial potential was optimized for flexible methanol. CH_3OH was described employing the general AMBER force field (GAFF) model.[88] The resulting radial energy profile affects mostly the molecules within ∼12 Å from the boundary, as can be inspected from the figure. Adapted from Raucci *et al.*, J. Comput. Chem. **41**, 2228–2239 (2020). Copyright 2020 Wiley Periodicals LLC.

$$W^n(\mathbf{P}^n, \mathbf{R}) = W_{disp-rep}(\mathbf{R}) + W_{elec}(\mathbf{P}^n, \mathbf{R}) + W_{cav}(\mathbf{R}). \tag{2}$$

W_{cav} is the cavitation free energy, accounting for the work required from the system to carve a cavity within the liquid, as function of the cavity shape and size. In our macrocanonical simulations, the cavity is fixed and there is no need to compute W_{cav}. W_{elec} arises from the Coulomb interactions (long-range) between the explicit system and the implicit solvent (bulk). This term is the one that actually accounts for the mutual polarization and depends not only on $\mathbf{R}$, but also on the electronic density of a given state, $\mathbf{P}^n$. The bulk molecules are implicitly described by the polarizable continuum model (PCM), and this energy contribution is computed with a self-consistent procedure where the electronic density and the implicit solvent are mutually polarized.[84–86] The first term in Eq. (2) is due to dispersion–repulsion forces, mostly important at short distances, so between the outermost explicit molecules and the bulk solvent. $W_{disp-rep}$ is described by a solvent-specific effective potential obtained by the procedure presented in Ref. 87. The overall $W_{disp-rep}$ parameterization can be found in previous published works,[55–58] and the quality of the $W_{dis-rep}$ potential has been extensively proved to be accurate for the dynamics of several ions and chromophores in protic solutions.[29,31,55–58,73,80] In Fig. 1, we report the $W_{disp-rep}$ potential profile optimized in Ref. 60 for the flexible methanol solvent. We wish to point out that this term is assumed to be independent by the electronic density of the state of interest, since its intrinsic short range. In Fig. 1, $W_{disp-rep}$ rapidly assumes negligible values already at short distances from the boundary, *r*, indeed. On the other hand, $W_{disp-rep}$ depends on the specific physical conditions, such as density and temperature, and on the solvent/matrix molecular model considered and is not generally transferable to other solvents/matrices.

B. Phase-space point sampling for photo-induced processes at finite temperature

Non-equilibrium photo-induced reactivity in solution at finite temperature can be strongly dependent on polarization effects and electrostatic interactions with the surrounding molecules that can strongly tune the energetic, the cross section, and the lifetime of photo-induced states.[28–35] Routinely used computational methods for optical properties and photo-induced reactivity rely on the study of solute–solvent clusters corresponding to energy minimum structures on the potential energy surface that are representative, on average, that is, of the dye microsolvation. Cluster approaches can be reliable to sample equilibrium time-independent quantities, but obviously the thermal equilibrium fluctuations are already lacking into equilibrium description provided by these clusters and definitively are required to observe in real time non-equilibrium evolution of excited states. The excess of energy, acquired by the system upon excitation, depends above all on how initially the overall energy was already distributed among the internal degrees of freedom and from where the system can reach the Franck–Condon region. This means that both initial positions and momenta, defining a point in the phase space, are important to achieve meaningful results. Not only the absolute values of kinetic and potential energies are crucial but is of paramount importance how these last ones are distributed among the degrees of freedom to translate the thermal equilibrium into the molecular picture. As a complementary approach, the configuration space sampling provided by molecular dynamics simulations may be a suitable choice to simultaneously obtain both these distributions and a reliable description of solvent effects along with solute chemical–physical properties, at finite temperature. This is even more important for the solvent, since it presents multiple time-dependent effects, such as solute–solvent vibrations and electrostatic interactions with bulk, kinetic energy distribution among multiple collective degrees of freedom (THz region).

Starting from a more rigorous treatment of such problem, the probability distribution for a generic system coordinate (Q) obeying to a harmonic potential is graphically reported in Fig. 2. The quantum distribution is different from that for a classical harmonic oscillator,

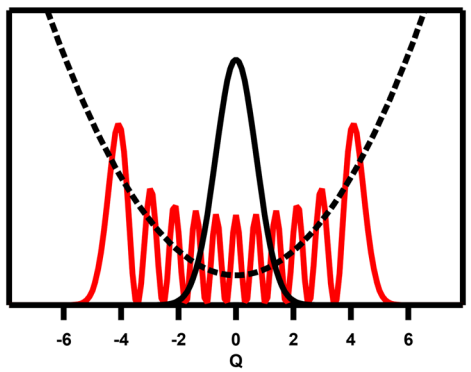

FIG. 2. Quantum probability distribution of a generic system coordinate (Q, arbitrary units) obeying to a harmonic potential. The quantum states with n = 0 (black solid line) and n = 10 (red solid line) have been chosen for example. The Q quantum probability distribution is very different from the classical distribution (represented as black dotted line), such difference decreases as soon the energy, and so n increases.

for which the most probable value for Q is found at the oscillator's classical turning points (with zero probability). The difference between the classical and the quantum distributions of Q decreases with an increase in energy. We require to obtain a function $S(Q, p)$, the classical probability density, which reproduces somehow quantum distributions in positions Q and momenta p, that obeys

$$\int\int S(Q,p)dQdp = 1. \tag{3}$$

Semi-classical approaches can be based on normal mode analysis and consequent sampling of the normal mode space. Thus, $S(Q, p)$ for small polyatomic systems can be obtained by orthant sampling,[89–91] microcanonical normal mode sampling,[92] fixed normal mode energies,[93–95] local mode sampling,[96] or sampling a Boltzmann distribution. The statistical phase-space theory,[97–99] intermediate-coupling probability matrix theory,[100] and information theoretic analyses[101–104] can be used also for this aim. All these previously mentioned methods require a small subset of degrees of freedom to focus on. A more interesting way to obtain $S(Q, p)$ and achieve accurate results for large systems ($\gtrapprox$1000 atoms) is from molecular dynamics simulations. MD simulations can be used to sample the $S(Q, p)$ distribution at ground-state (GS) equilibrium. Thus, proper initial conditions (both atomic coordinates and momenta) are chosen from this distribution for the swarm of trajectories to be propagated into the excited state of interest. This approach allows us to explore a more significant part of the Franck–Condon region accessible at finite temperature upon excitation. Usually, quasi-classical sampling methods are widely used to select initial conditions for classical trajectories. These methods require expensive on-the-fly calculations of energies, forces, and couplings between the electronic states (for non-adiabatic phenomena). These computational bottlenecks are usually avoided by using model Hamiltonians, semi-empirical and tight binding methods, or reduced dimensionality PESs to study non-adiabatic light-induced system evolutions. However, a different approach is still demanded for studying ultrafast photo-induced reactivity and non-equilibrium relaxations right upon excitation in a system embedded in a complex environment, where a large part of the degrees of freedom are required to be treated explicitly to achieve the right accuracy. Protocols relying on hierarchic computation schemes that are capable to describe in both explicit and accurate ways the weak interactions for a still reasonable large part of the system, simultaneously including the bulk electrostatic and dispersion forces, are in our opinion very promising in this field. Thus, several case studies and *ad hoc*-developed computational protocols for treating the effects of the environment, on both the first-principles potential evaluation and the phase-space sampling at finite temperature, are highlighted and presented in this review.

III. ULTRAFAST PHOTO-INDUCED PROCESSES: ACCURATE SOLUTE–SOLVENT POTENTIALS AND BIAS/CHOICE OF THE COORDINATES TO FOLLOW DURING THE RELAXATION

A. Simulation of the time-dependent optical emission of a solvatochromic dye in solution at room temperature

Sub-picosecond timescale ultrafast modifications of specific solute–solvent interactions, such as a changes around solvation sites due to the solute electronic excitation, can be detected by time-resolved

fluorescence signals.[105–109] In this paragraph, we recall the ultrafast photo-emission experiment of a chromophore in water solution, N-methyl-6-oxyquinolinium betaine [MQ; see panel (a) in Fig. 3], characterized by a large change of polarity and H-bond ability between the ground and the excited states.[80] DFT and molecular mechanics potentials were combined on the fly employing the N-layered integrated molecular orbital and molecular mechanics (ONIOM) QM/MM methodology.[110–113] The so-called electronic embedding scheme, by including the MM charges in the QM Hamiltonian, was used to describe the QM/MM electrostatic interactions. NPBCs were used to accurately describe both electrostatic and dispersion contributions (important at long and short distances, respectively) coming from the interactions between the explicit molecules and the implicit bulk. DFT and TD-DFT were employed for describing the ground and first singlet excited state, respectively, by solving the Kohn–Sham equation using the global hybrid Becke, 3-parameter, Lee–Yang–Parr (B3LYP) density functional[114–117] and the 6–31 G(d,p) basis set. The solute is centered at origin of a sphere, where three solvation shells are explicitly treated via TIP3P[118] water model. On these solid grounds, an accurate *ab initio* dynamics[119–121] of the MQ in water solution at room temperature was collected for providing a molecular interpretation of the Stokes shift dynamics and sub-picosecond non-equilibrium relaxation of the system suddenly after the absorption. A semi-classical approach was used, where the emission spectrum is simulated by computing the evolution toward the new equilibrium of a swarm of excited-state *ab initio* MD trajectories starting from the ground-state configuration distribution, $\rho(Q, t)$. The resulting time evolving signal is reported in panel (c) of Fig. 3. For this aim, we chose a reasonable number of initial starting points from the ground-state room-temperature MD for sampling $S(Q, p)$ at time zero of the excitation. The strategy was to select 24 points from the phase space sampled during the S_0 MD to represent the MQ–water system at the starting time of the Stokes shift dynamics, each collecting the relaxation process from a possible Franck–Condon nuclear configuration caught up with the electronic excitation. Initial points in the phase space for accurately sampling the Franck–Condon region were selected by gauging these quantities: (i) the $E_{S1\leftarrow S0}$ transition energy average and distribution were very close to the steady state $S_1 \leftarrow S_0$ absorption peak and bandwidth; (ii) the E_{kin} initial nuclear kinetic energies reproduced the S_0 average total linear momentum. The $E_{S1\leftarrow S0}$ energies and E_{kin} values for all initial phase-space points are summarized in Table I. The starting configurations have been further analyzed to ensure the proper representation, on average, of the S_0 structural properties. In Table II are analyzed in detail the average MQ-first-shell water interactions by inspecting: (i) the distance between the MQ solvation site (the oxygen) and the water oxygen (O.O) or the water hydrogen (H.O); (ii) the water oxygen, the water hydrogen, and the MQ oxygen angle (H–O.O); and (iii) the hydrogen bond number with the solute solvation site (N_{HB}, thresholds of 2.7 Å, 3.5 Å, and 30° for the O_{MQ}–H_{wat} distance, the O_{MQ}–O_{wat} distance, and the H_{wat}–O_{wat}–O_{MQ} angle, respectively). The selected points resemble the radial distribution function (RDF) integration and peak maxima for S_0 water–MQ interactions, as can be inspected in panel (d) of Fig. 3. Stokes shift time evolution was simulated for 4000 fs, and the dipole strength and the vertical excitation energy toward the first singlet excited state were collected as well during the dynamics. MQ upon excitation [please see HOMO and LUMO isodensity plots in panel (a) of Fig. 3] has a drastic change in the solute–solvent-specific interactions within 4 ps [a neat loss of ∼1.4 water molecules can be inspected in the solvent spatial distributions and in the RDF, reported in panels (b) and (d) of Fig. 3, respectively]. Even if the solute experienced a drastic

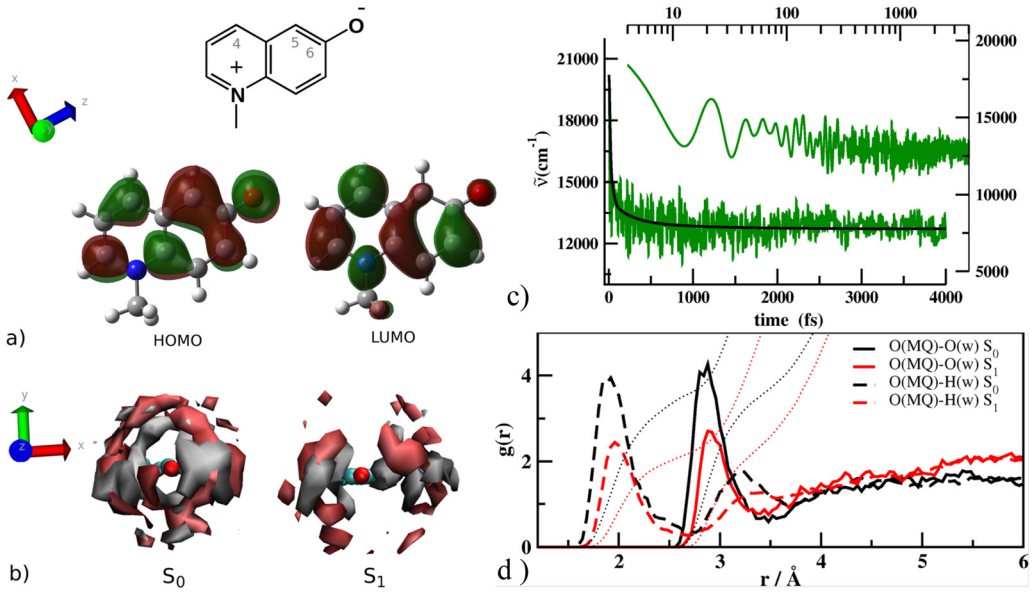

FIG. 3. (a) N-methyl-6-oxyquinolinium betaine (MQ) Lewis structure and HOMO and LUMO B3LYP/6-31G(d,p) isosurfaces. (b) 3D spatial orbitals indicating the average positions of oxygens and hydrogens for the ground (left) and first singlet (right) AIMDs in red and gray, respectively. (c) Simulated emission signal in time (wavenumbers, in green) of the MQ in water, obtained as average TD-DFT energy from the first singlet excited-state trajectories. The data resemble a clear exponential decay, and a fit is reported in black. (d) RDFs of water oxygens and hydrogens relative to the MQ solvation site (oxygen) obtained from the analysis of the ground and excited-state AIMDs; see figure for the legend. Adapted from Petrone *et al.*, J. Amer. Chem. Soc. **136**, 14866–14874 (2014). Copyright 2014 American Chemical Society.

TABLE I. $S_1 \leftarrow S_0$ transition energies (eV) and nuclear kinetic energies (a.u.) for the initial phase-space points chosen for the excited-state swarm of trajectories, labeled by Roman numbers. Adapted from Petrone *et al.*, J. Amer. Chem. Soc. **136**, 14866–14874 (2014). Copyright 2014 American Chemical Society.

ID	$E_{S1\leftarrow S0}$	E_{kin}	ID	$E_{S1\leftarrow S0}$	E_{kin}
I	2.66	0.581 744	XIII	2.56	0.583 965
II	2.43	0.584 196	XIV	2.48	0.581 949
III	2.71	0.587 116	XV	2.37	0.571 105
IV	2.65	0.585 087	XVI	2.51	0.583 391
V	2.54	0.579 310	XVII	2.62	0.578 966
VI	2.43	0.584 196	XVIII	2.40	0.574 540
VII	2.53	0.579 158	XIX	2.27	0.575 237
VIII	2.38	0.583 965	XX	2.54	0.573 252
IX	2.43	0.568 866	XXI	2.29	0.581 899
X	2.36	0.586 163	XXII	2.45	0.588 840
XI	2.36	0.581 949	XXIII	2.51	0.569 375
XII	2.50	0.581 633	XXIV	2.41	0.572 673

decrease in hydrogen bond interactions following the excitation, the proposed computational approach is capable of highlighting the clear dependence of Stokes shift dynamics from large amplitude collective water motions in THz frequency domain. The adopted methodology to define the potential energy surfaces was able to accurately describe the hydrogen bond structure and energetic, in both the ground and the excited electronic states. These results explain how the time-dependent Stokes shift of the MQ solvatochromic dye [reported in panel (c) of Fig. 3] can be disentangled in terms of IR and THz frequency contributions to the solvent reorganization. This case study provided a strong validation of the potentials, the phase-space sampling, and the choice of the initial conditions, given the nice agreement with the fluorescence lifetime and dynamics.

TABLE II. Structural parameters (Å and °) and hydrogen bond number involving the MQ oxygen and the first solvation shell for the MQ/water initial phase-space points chosen for the excited-state swarm of trajectories. Adapted from Petrone *et al.*, J. Amer. Chem. Soc. **136**, 14866–14874 (2014). Copyright 2014 American Chemical Society.

ID	H..O	O..O	H–O..O	N_{HB}	ID	H..O	O..O	H–O..O	N_{HB}
I	2.192	3.119	13.48	4	XIII	2.129	3.065	14.06	3
II	1.860	2.848	6.13	4	XIV	2.045	2.870	20.77	3
III	1.946	2.895	5.81	4	XV	2.219	3.071	21.14	3
IV	2.136	2.998	19.43	3	XVI	2.280	3.105	21.87	3
V	2.265	3.084	21.54	4	XVII	2.224	3.116	15.80	3
VI	1.860	2.848	6.10	4	XVIII	2.299	3.238	12.39	3
VII	2.090	3.005	5.86	4	XIX	2.312	3.108	23.34	3
VIII	2.396	3.260	19.23	3	XX	2.224	3.104	17.94	3
IX	2.213	3.091	19.32	3	XXI	2.224	3.097	17.08	3
X	2.186	3.042	21.22	3	XXII	2.223	3.156	14.72	4
XI	2.232	3.086	21.41	3	XXIII	2.304	3.083	25.22	3
XII	2.288	3.109	20.71	3	XXIV	2.260	3.196	10.37	3

B. Ultrafast excited state proton transfer reaction of a superphotoacid in solution

Simulation of strong photoacidity in solution is a brilliant example of the importance of choosing the right combination of accurate potential and ground-state phase-space sampling to capture the main features of an ultrafast process. Here, we highlight the interesting ultrafast excited state proton transfer (ESPT) reaction of the quinone cyanine 9 (QCy9), a superphotoacid in water solution, reported in Fig. 4.[122] This photoacid exhibits a dual-band emission in aqueous solution arising from the photoprotolytic reaction: a relatively weak short-wavelength emission band at about 480 nm is attributed to the protonated form, while a high-intensity band peaked at about 680 nm originates from the deprotonated one. The fluorescence upconversion signals, measured at 700 nm, show a fast rise time component, with a time constant of about 100 fs, attributed to the ESPT toward the aqueous solvent.[123] The complexity of this type of photo-induced phenomenon arises because a wide range of time and spatial scales are in play: starting from chromophore excitation to arrive to the final proton motion across the solvent, passing via a proton transfer complex formation. Other difficulties need to be taken into account, such as the excited chromophore electron density rearrangement, showing a substantial charge transfer (CT) character.

The QCy9 dye ground (S_0) and excited (S_1) state potentials were obtained setting up the model described in Sec. II. For this aim, the QCy9 molecule was embedded in 608 water molecules and centered in a sphere of radius 16.5 Å (for more details, please refer to Ref. 122). The B3LYP functional was adopted for the ground-state MD, while CAM-B3LYP[124] was chosen for the excited-state simulations. In S_0 MD, QCy9 and water molecules were treated at QM and MM level, respectively. From this sampling, we obtained significant insight about the equilibrium QCy9 structure and the hydrogen bond (HB) network in which the proton acceptor water molecule (W_1) is involved. For instance, the QCy9 dye shows soft dihedral angles governing the main skeleton arrangement, although an approximately planar structure is adopted on average. Regarding the cybotactic region, the W_1 water molecule solvates the QCy9 OH group and acts as HB acceptor from other water molecules for 42% of the time while, for the remaining time, its lone pair electrons are involved only in the HB with the QCy9 hydrogen. Regarding non-equilibrium dynamics in the photo-induced excited state, the accuracy of the simulation depends on the correct setup of the QM/MM layout, which is crucial to describe the solute–solvent and solvent–solvent-specific interactions. The main point of the QM/MM calibration is to establish the correct number of solvation shells that have to be included in the QM space to describe the ESPT event correctly. Trial S_1 trajectories were collected starting from an initial configuration (IC_1) representing the average of the QCy9 cybotactic region, in particular the arrangement of the proton acceptor water molecule W_1. These S_1 trial dynamics were performed with a different number of water molecules included in the QM region along with the QCy9 solute and unequivocally demonstrated that the PT event could occur only when three shells of solvation around W_1 are treated at QM level. This enlarged QM/MM layout was then used to simulate the S_1 relaxation with two further initial configurations (IC_2 and IC_3), mimicking several topologies of the W_1 microsolvation. In the IC_1 configuration, representing the average situation, a strong interaction passes between the QCy9 acid group and the W_1 acceptor, with two other water molecules engaged in stable HBs with W_1. The IC_2 and

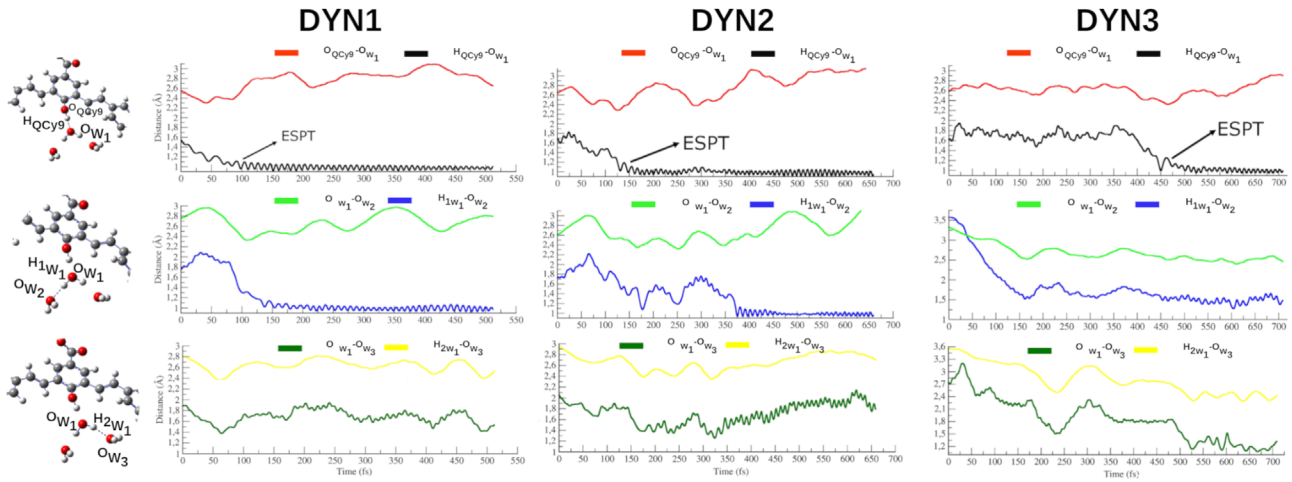

FIG. 4. From top to bottom panels: Ball and stick representations and S_1 dynamics of the QCy9 acidic proton and the nearest water molecules. The monitored structural parameters are highlighted for each hydrogen bond donor–acceptor couples: QCy9-W1, W1-W2, and W2-W3. Oxygen, carbon, and hydrogen atoms are presented in red, gray, and white, respectively. Plots reporting their time evolution for DYN1, DYN2, and DYN3 trajectories are progressively depicted from left to right. Please see figure color legend (on top of each panel) for defining the investigated structural parameters and refer to the main text for the trajectories labeling schemes. From the plots is clear that the excited-state proton transfer process occurs within the first 150 fs for DYN1 and DYN2, while is about three times slower for the DYN3 case. Adapted from Raucci *et al.*, J. Chem. Theory Comput. **16**, 7033–7043 (2020). Copyright 2020 American Chemical Society.

IC_3 configurations differ by how the W_1 first solvation shell is modeled; namely, W_1 is strongly H bonded with one further water molecule, while IC_3 presents weak HBs between W_1 and the surrounding solvent. The main structural parameters describing the HB network are reported in Table III.

The resulting S_1 trajectories, starting from IC_1, IC_2, and IC_3, are labeled DYN1, DYN2, and DYN3, respectively, and in Fig. 4, the time evolution of important structural parameters describing the ESPT is reported in the three cases. As can be observed, the ESPT mechanism is strictly dependent on the HB dynamics of the first solvation shell around the proton acceptor molecule. It is worth noting that in the case of DYN3, namely, the dynamics from a starting configuration with weak W_1-water HBs, the ESPT takes place on a longer time at about 500 fs. Indeed, the first part of the trajectory is spent to reach an optimal and stable pattern of HBs between W_1 and its solvation shell that is necessary to promote the PT. In the case of the DYN1 and DYN2, on the other hand, this preparatory step is not required, and the ESPT takes place immediately, representing the situation where the HB network around W_1 is already capable to support a PT complex stabilization, and the photoreactivity can occur right after the photoexcitation. In these cases, the ESPT happens at about 100 fs. In all of the cases, the timescale is comparable to the experimental one, this result being consistent with an accurate modeling of ESPT process.

TABLE III. Main structural parameters (Å) for the starting configurations ($IC_1 - IC_3$) of the excited-state molecular dynamics simulations.

	IC1	IC2	IC3
O_{QCy9}-O_{W_1}	2.552	2.646	2.588
O_{QCy9}-O_{W_1}	1.548	1.692	1.623
O_{W_1}-O_{W_2}	2.757	2.616	3.643
O_{W_1}-O_{W_3}	2.807	2.954	2.952
O_{W_1}-O_{W_4}	2.909	3.362	3.076

C. Ultrafast vibrational dynamics

1. Vibrational relaxation of the pyranine molecule in aqueous solution

Vibrational dynamics is generated by the out-of-equilibrium evolution of forces among nuclei upon the phototriggered rearrangement of the electronic density and is the key information to understand the forces driving toward photoreactivity, conical intersections, nonradiative decays, etc. When a single potential energy surface is capable to describe the relaxation, the vibrational dynamics also evolves into the new equilibrium vibrational states in terms of excited-state normal modes. The time employed to reach this new equilibrium is also important to understand the new chemistry adopted in the excited state. Nowadays, high-resolution time-resolved femtosecond stimulated Raman spectroscopy (FSRS) and attosecond transient absorption spectroscopy allow us to probe in real-time photo-induced reactions on the timescales of the nuclear and electronic motions.[125–129] FSRS is a powerful technique capable to unveil nuclear–electronic coupling occurring with electronic density redistribution.[130–132] Despite the enormous potential of these techniques, the correct signal interpretation is still a source of debate.[48,75] On the other hand, the simulation of the vibrational dynamics requires an highly accurate computational method, capable to describe the time evolution of the quantum wave packets relaxing after the excitation.[133–136] Such methods are not feasible for large-sized molecules in condensed phase. The classical approach, on the other hand, allowing for detecting vibrational dynamics from *ab initio* molecular dynamics, is in principle doable but needs to rely on highly accurate energy potential, and an accurate

representation of the equilibrium vibrational state in the ground state and the right evolution after the excitation. We discuss here the setup of such a method to investigate the ultrafast vibrational dynamics in the emblematic case of the 8-hydroxypyrene-1,3,6-trisulfonic (HPTS or pyranine) molecule in water solution. Pyranine is a widely studied weak photoacid[137–139] where the ESPT occurs with time constants of 3 and 90 ps.[140] Off- and on-resonance FSRS study revealed a rich and complex transient (sub-picosecond scale) vibrational dynamics, with a sequential activation and decay of low-frequency ($<1200\ cm^{-1}$) skeleton modes[140,141] that precede and possibly prepare the ESPT reactive event.

Hessian-based vibrational analysis requires the localization of a representative energy minimum on the PES. The high computational cost for large systems like molecules in the condensed phase makes these methods inapplicable.[142,143] Generalized vibrational modes defined from AIMD come in handy in this case.[119,120] This approach relies on the assumption that, at any temperature, a set of 3N generalized molecular modes Q, conjugate to uncorrelated linear momenta, can be defined. The method's strength relies on the inclusion of environment effects and the intrinsic anharmonicity related to molecular motions.[144] Therefore, explicit solvent models can be exploited,[55–57] and the methodology is successfully adopted for vibrational analysis of molecules at equilibrium.[58,80,145] This analysis has been extended to far from equilibrium process, giving major insight about transient vibrational signals activated in the relaxation process in the electronic excited state (ES). Briefly, the protocol relies on the assumption that excited mode composition right after the excitation, that is, when relaxing ultrafast in the Franck–Condon region, can be assumed to be the same as in the ground state (GS). In this way, one can obtain the ES velocity vector by projecting mass-weighted velocity along with the previously obtained GS modes. Vibrational frequency values along the time are obtained by multiresolution vibrational analysis based on the wavelet transform.[146–151]

Our method was applied to study a window of 1 ps after the electronic excitation of the pyranine in water solution. As soon as vibrational relaxation rules the Raman activity over time, the precedently illustrated vibrational analysis can retrace the timing and patterns of Raman signals. After the S_0 sampling, we started five ES dynamics starting from five different initial configurations. In principle, the number of ES trajectories should provide a reasonable and statistically valid representation of the distribution of phase-space points sampled at thermal equilibrium. We focused here on 6 N normal-like vibrational coordinates and momenta. In this circumstance, a moderate number of trajectories sampled from points belonging to the FC region are reliable for small-sized molecules. In particular, we selected the starting points on the base of the pyranine C–C distances close to the ground-state average values. Finally, from radial distribution functions,[73] we observe that the HPTS phenolic group shows a hydrogen bond with a water molecule in all five configurations. Hessian-based harmonic frequency calculations on pyranine minima for the excited and ground electronic state in implicit aqueous solvent were performed.[73,152,153] In the following, we illustrate the ES vibrational analysis. A particular focus is made on those vibrational bands that are characterized, in accordance with off-resonance FSRS data, by complex dynamics. It should be stressed that the protocol can correctly describe the appearing and disappearing of signals in a tangled temporal sequence of femtoseconds. This timescale is associated with the time for the pyranine to complete the first important structural rearrangement after the photoexcitation.[73,154] All modes have a collective nature, involving the four rings of the aromatic system motion. We focused on modes at about 950 and 630 cm^{-1} that represent the ring deformation. Figure 5 summarizes the analysis of these modes where the generalized mode composition is shown on the right panel. In distinction, the wavelet spectra corresponding to excited-state mode velocities are reported on the left panel as 2D maps. Due to the absence of signals of relevant intensity over generalized mode frequencies, values between 0 and 2000 cm^{-1} are analyzed. In Fig. 5(a), right panel, a generalized mode that describes an in-plane ring deformation with a significant hydrogen out-of-plane component is reported. It coincides with the harmonic, S_1, normal with a calculated harmonic frequency of 970 cm^{-1}. We are also able to interpret the corresponding vibrational band observed at 950 cm^{-1} by FSRS.[154] As can be verified by the wavelet spectrum in Fig. 5(a), left panel, an isolated band centered at 950 cm^{-1} initiates to ascend after 100 fs and to decay after 600 fs from excitation. Also, in this case, we can observe an excellent accordance with experimental data like kinetics rise and decay constants, respectively, of 140 and 600 fs. Focusing on Fig. 5(b), the reported generalized mode results from a combination of ring wagging and breathing modes with in-plane and out-of-plane ring deformations. This mode matches the mode obtained from static calculations with harmonic frequency at 660 cm^{-1} and corresponds to the FSRS signal recorded at 630 cm^{-1}. Also in this case, we have a good agreement with an experimental rise time of 300 fs. This mode presents a decay time longer than 1ps with intensity oscillating over the time. Since the intrinsic anharmonicity, responsible for coupling low and high-frequency modes in time-resolved vibrational signals,[153,155] a wide range of signals, with different frequencies, can be observed in the wavelet spectrum. In summary, thanks to the excellent agreement between the experimental pyranine rise and decay kinetics timescale and the presented results, we proved that a wise choice of the energy potential and initial configurations, for the excited-state dynamics, in synergy with the presented computational strategy, can provide an accurate picture of the intricate vibrational dynamics of pyranine in aqueous solution.

2. Relaxation dynamics of a non-covalent charge transfer complex in solution

Vibrational dynamics is particularly important to follow the photo-induced relaxation of non-covalent intermolecular CT complexes. Here, we discuss the case of the CT complex formed by 1-chloronaphthalene (1ClN), acting as electron donor, and the tetracyanoethylene (TCNE)[156–158] molecule (the electron acceptor; see Fig. 6, top panel). Ground-state properties and, mostly important, the low-lying CT electronic transition have been addressed in detail and compared to experimental spectroscopic data.[72,159,160] The main interactions ruling the complex structure are non-covalent in nature and are responsible of the observed π–π stacked arrangement in polar aprotic solvents[161] such as dichloromethane (DCM). The model and the protocol described in Sec. II have been adopted to characterize the ground state and the relaxation in the first singlet excited state, while the vibrational dynamics has been studied through the multiresolution wavelet protocol introduced in Subsection III C 1.[48,73,80,144,155,162–165] In this manner, we obtained useful insight on the internal vibrational

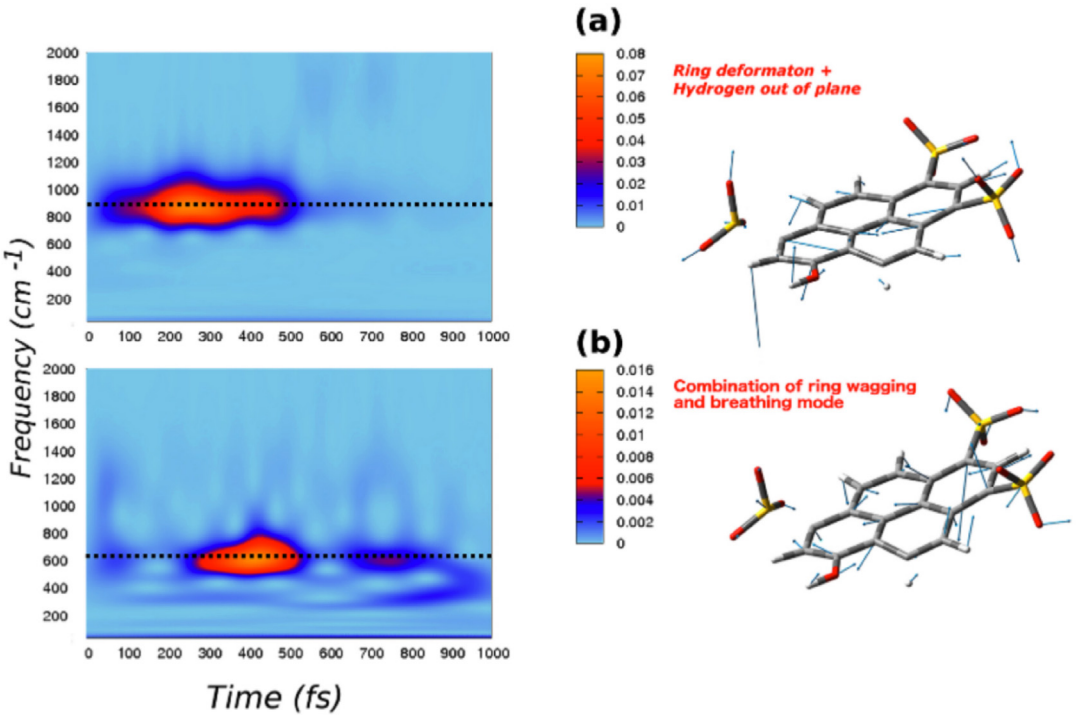

FIG. 5. Generalized modes (right panel) and related 2D wavelet power spectra (left panels). The color scale accounts for the power spectra magnitude (in arbitrary units): (a) coupled ring deformation mode and hydrogens out-of-plane motion, with an AIMD frequency of 930 cm^{-1} and an exp. value of 952 cm^{-1}. Exp rise and decay time of 140 and 600 fs (from Ref. 154) and (b) ring wagging combined with a breathing mode, with an AIMD frequency of 620 cm^{-1}, an exp. value of 630 cm^{-1}. Recorded exp. rise time of 300 fs. Adapted from Chiarello *et al.*, J. Chem. Theory Comput. **16**, 6007–6013 (2020). Copyright 2020 American Chemical Society.

energy flow following the electronic excitation, translating the relaxation process in terms of anharmonic nuclear motions and anharmonic vibrational couplings over the time. We mainly focused on the role played by selected vibrational modes in promoting the relaxation from the CT state (S_1) to the S_0 ground state.[72]

Molecular systems mainly ruled by Coulombic and van der Waals interactions are particularly challenging to model from a computational point of view because of a large conformational space that can be explored and the numerous stationary points that are equally populated at k_BT thermal energy. The potential energy hypersurface of a non-covalent molecular complex is then very difficult to describe, possibly showing a large number of energy minima almost degenerate for which the definition of one or few representative equilibrium structures becomes meaningless. Therefore, regarding the characterization of the equilibrium ground state, our efforts focused on the accurate description of non-covalent interactions. The good agreement between the calculated vertical excitation energies and the absorption spectrum measured in DCM solution was considered as validation of the modeling strategy undertaken. Then, the coordinates of the TCNE:π:1ClN minimum energy structure optimized in dichloromethane solvent were chosen as starting point to run a 10 ps-long AIMD. The atom-centered density matrix propagation (ADMP) formalism was adopted.[55,59,79,119–121,166,167] It was reasonable to expect that the nuclear evolution on the S_0 potential energy surface would have taken place through very low energy barriers and that flat regions could have been easily populated. As a matter of fact, we found several isoenergetic (within less than 1 kcal/mol) π-stacked conformers in solvent. In these structures, the planarity of both monomers and the face-to-face arrangements were always observed, with the TCNE monomer sliding on the 1ClN molecular plane and slightly reorienting.

A careful analysis of the S_0 phase space was performed to choose initial coordinates and momenta to sample the relaxation in the CT state potential energy surface. We extracted ground-state configurations showing the lowest deviations of the vertical excitation energy from the experimental spectrum. We also considered representative values of distances between the two monomer centers of mass centers. Finally, we analyzed the CT extent in these structures through a natural bond orbitals (NBO)[168–172] analysis. In Fig. 7, we report the three chosen configurations along with a summary of the considered properties.

Excited-state AIMD simulations were performed in implicit DCM solvent for about 6 ps on the first singlet electronic state. We then analyzed the S_1 trajectories in order to unveil the role of key vibrational modes and their coupling leading downhill the Franck–Condon region. Moreover, we focused on possible vibrational motions contributing to the activation of non-radiative relaxation channels of the CT complex from the S_1 to S_0 state. For an accurate identification of the vibrational modes that govern the photo-relaxation of the CT complex, we relied on the calculation of TD-DFT energy scans and the evaluation of the first-order non-adiabatic coupling (NAC) matrix elements[74,173] for structures slightly displaced of a small δ increment along each vibrational mode of interest.[72] The main

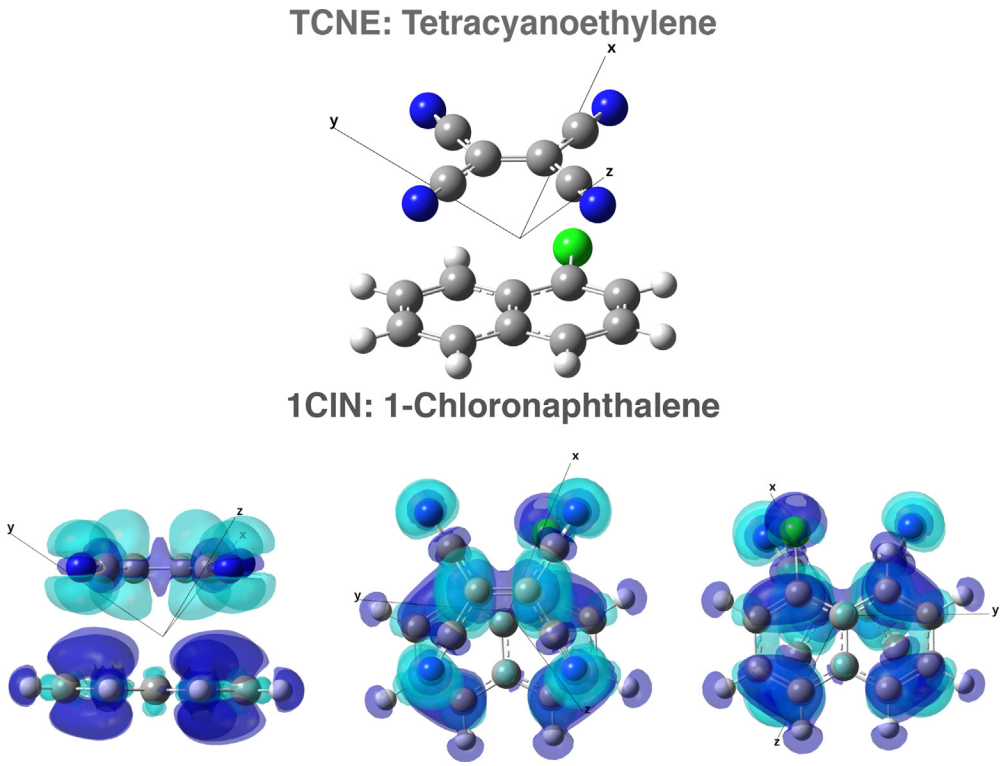

FIG. 6. Top: TCNE:π:1ClN charge transfer complex. Bottom: Positive and negative variation of electronic density ($\Delta\rho$) in light and dark blue, respectively, associated with the first electronic transition with a charge transfer (CT) character. Adapted from Coppola *et al.*, Chem. Sci. **12**, 8058–8072 (2021). Copyright 2021 The Royal Society of Chemistry.

results are summarized in Fig. 8. In particular, three excited-state vibrational modes are proved to be the main relaxation channels that lead the entire non-covalent complex to the fundamental electronic state. In Fig. 8, panel (a) we report the TD-DFT profiles and the NACs calculated along the normal coordinates of a low-frequency mode mainly localized on the TCNE electron acceptor. The ΔE values show a bell-shaped trend, on the sides of the Franck–Condon geometry ($\delta = 0$ at 1.93 eV), and a decrease in the energy gap between S_0 and S_1

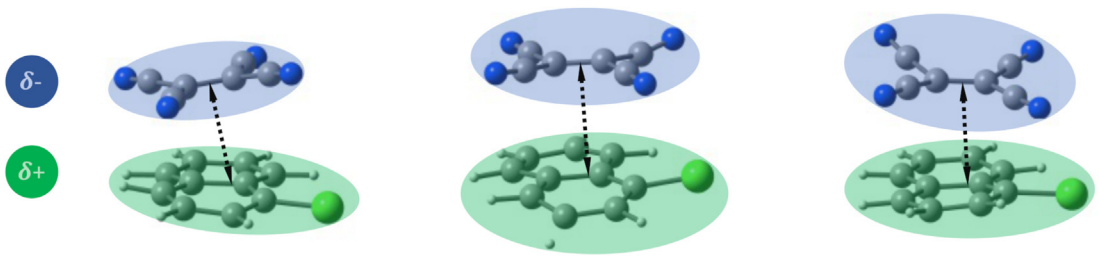

C.o.M	3.617 Å	3.839 Å	3.963 Å
$S_1 \leftarrow S_0$	2.08 eV (0.23)	2.07 eV (0.24)	2.26 eV (0.05)
$S_2 \leftarrow S_0$	3.10 eV (0.06)	2.97 eV (0.07)	2.89 eV (0.15)
NBO S_0:	±0.078 *e*	±0.020 *e*	±0.033 *e*
NBO S_1:	±0.807 *e*	±0.948 *e*	±0.917 *e*

FIG. 7. Initial configurations of excited-state BOMD simulations, extracted from ground-state AIMD. Values of the center of mass distances (C.o.M, Å) between the two monomers, vertical excitation energies (eV, absolute errors vs experimental ones in parenthesis), and the total NBO charge (*e*) for each subunit in the ground (S_0) and first singlet excited state (S_1, CT character) are reported. Adapted from Coppola *et al.*, Chem. Sci. **12**, 8058–8072 (2021). Copyright 2021 The Royal Society of Chemistry.

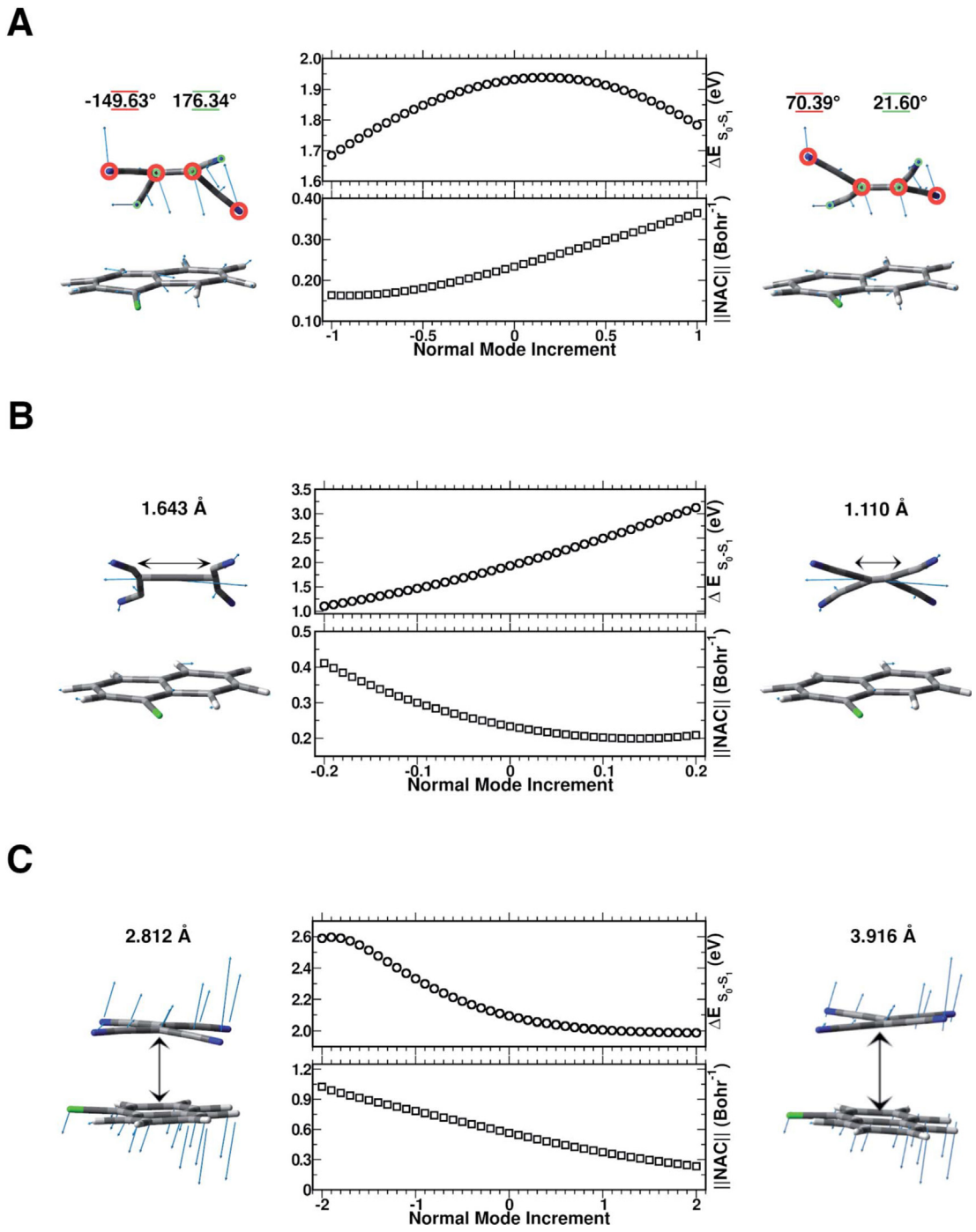

FIG. 8. Panel (a), left and right columns: Geometries displaced with respect to the equilibrium position along the normal mode involving the NC=CN dihedral angles (highlighted by red and green circles); center top and bottom: $S_1 \leftarrow S_0$ vertical excitation energies (eV) and Frobenius norm of non-adiabatic coupling matrix (in $bohr^{-1}$) computed along the normal mode increment, respectively. Panel (b), left and right sides: Maximum displacements with respect to the equilibrium position of the normal mode including the C=C bond length; center top and bottom: $S_1 \leftarrow S_0$ transition energy (eV) and Frobenius norm of non-adiabatic coupling matrix (in $bohr^{-1}$) computed along the normal mode increment, respectively. Panel (c), left and right sides: Maximum displacements with respect to the equilibrium position of the normal mode including the variation of center of mass distance between the two subunits; center top and bottom: $S_1 \leftarrow S_0$ transition energy (eV) and Frobenius norm of non-adiabatic coupling matrix (in $bohr^{-1}$) computed along the normal mode increment, respectively. Adapted from Coppola *et al.*, Chem. Sci. **12**, 8058–8072 (2021). Copyright 2021 The Royal Society of Chemistry.

states is observed. On the contrary, however, the NAC values show a rapid increase (up to 0.365 in $bohr^{-1}$) only for positive increments, that is, when the central C = C moiety of the TCNE is closer to the donor monomer, thus suggesting that this motion is particularly involved in the relaxation dynamics.

Following the photoexcitation, the C = C bond distance is remarkably stretched out (on average from 1.374 Å in S_0 to 1.433 Å in S_1) implying that the local electronic density is strongly reorganized upon the interaction with the external field. This peculiar behavior motivated us to investigate in detail the role played by the stretching mode on the central core of the TCNE molecule. Referring to Fig. 8, panel (b), in this case a clear correlation is observed between the C = C distance and the adiabaticity degree between the two electronic states. Starting from the resting geometry, when the carbon pair assumes the maximum distance, greater than 1.5 Å, the S_0–S_1 energy gap reaches the minimum value (−0.83 eV) allowing a significant approach of the PESs that are gradually more coupled as shown by the high positive slope of the NAC norm (0.411 in $bohr^{-1}$ at $\delta = -0.2$). On the contrary, the approach of the two carbon atoms along the internuclear axis involves a strong energetic separation of the PESs and a notable decoupling. To sum up, these data unambiguously indicate that the C = C double bond is a very sensitive probe of the photo-induced CT extent representing an effective reaction coordinate in non-radiative relaxation more efficient than others. To further confirm, for this specific vibrational motion we calculated the bivariate normal distribution between the TCNE C = C bond length sampled in the excited state and the electronic energy gap of the two electronic states, and it is emphasized that for high bond distances the $\Delta E_{S_0-S_1}$ moves toward its lowest value. It is worth pointing out that the computational protocol employed here allowed us to precisely assign the frequency of 1485 cm^{-1} to the C = C stretching localized on the TCNE unit and the feature at 1391 cm^{-1} to one of the C–C stretching modes on the naphthalene portion. It is well known that the intermolecular plane distance can play a decisive role in non-covalent molecules especially when photoexcited in terms of frontier molecular orbital overlaps and electronic couplings. For this purpose, we extracted the vibrational frequency underlying the center of mass distance. A low-frequency mode, rigidly approaching the two subunits one another, can be recognized [see Fig. 8 panel (c)]. Both the TD-DFT energy scan and the NAC calculations showed that following the approach of the two molecular planes, the energetic separation of the ground and the first excited state of the CT character is significantly influenced. In contrast, when the two planes are at a greater distance along the normal coordinate, we observe a smooth lowering of the excitation energy with a consequent decrease in non-adiabatic couplings with an evident negative slope.

Taking into account the challenging nature of the systems investigated in this work, our computational protocol proves to be reliable, general, and robust even for non-covalent species in the excited state. It is noteworthy to point out that in addition to a refined identification of the main excited-state vibrational modes and their anharmonic frequencies, through the multiresolution wavelet protocol we were able to observe their temporal evolution during the photo-relaxation as well as the vibrational couplings between small and large amplitude modes. We have also new important insight about the relaxation mechanism, and also, we were able to improve the experimental vibrational frequency assignment of the main vibrational mode that plays a key role in molecular relaxation. The robust and increasingly accurate theoretical–computational tools available today can be wisely used to rationally address the design of new molecules and to have a detailed understanding, on the atomistic scale, of out-of-equilibrium phenomena such as photophysics and photochemistry not easily attainable experimentally.

D. The challenging case of green fluorescent protein (GFP)

The green fluorescent protein (GFP) represents a widely studied topic in the scientific community because of the huge interest in its many applications, for example, in cell biology where it importantly redefined fluorescence microscopy, or live cell imaging experiments.[174–176] GFP has been used in modified forms to make biosensors and has been expressed in many species such as bacteria, yeasts, fungi, fish, and mammals. The large variety of applications has driven toward the engineering of many different GFP mutants allowing to obtain, among the others, the blue, yellow, red, and cyan fluorescent proteins.[177–179]

A full understanding of the photo-induced behavior of GFP still represents a challenge on a computational point of view since a correct description of the electronic excited states is not straightforward given the large size of the system that requires to combine both a correct description in terms of the chosen theory level and also a proper handling of the non-equilibrium electronic states as described in Subsections III D 1 and III D 2.

1. GFP structure and optical behavior

The so-called wild-type GFP from jellyfish *Aequorea victoria* is a 238 amino acid protein arranged in a β barrel structure. The chromophore p-hydroxybenzylideneimidazolinone (HBDI) is autocatalytically formed by the tripeptide Ser65-Tyr66-Gly67 and is responsible of the optical features presented by the protein. The protein environment is essential for the fluorescence of the chromophore; indeed, it is not observed in solution, where the chromophore mainly exists in its non-ionized form. The optical absorption of HBDI, mostly present in its neutral form in the electronic ground state,[180] is characterized by a major peak at 395 nm, while the fluorescence is observed at 508 nm, due to the ionic form of the HBDI.[180] Indeed, after the excitation, an ESPT takes place involving the chromophore, a crystallographic water molecule, Ser205 and Glu222 residues [see panel (b) of Fig. 9]. The photo-reaction starting from the chromophore has the Glu222 as final acceptor and shows a biphasic kinetics of 3 and 10 ps.[180–184] Aspects such as the driving forces, the mechanism, and the kinetics of the GFP ESPT are, until now, characterized by a not unique explanation in the scientific community.[185–187] Based on FSRS experiments performed by Mathies and co-workers, the role of a photoexcited low-frequency mode involving the chromophore was hypothesized to be involved in favoring the ESPT, by allowing the approach of the chromophore to the hydrogen bond network.[130] However, the key role of this low-frequency mode was not highlighted in other experimental studies.[188,189]

Static computational studies focused on the elucidation of the ESPT mechanism at different theory levels ranging from higher order wavefunction-based methods[190–193] to DFT also combined with molecular mechanics approaches (QM/MM)[194,195] have been performed in these years. *Ab initio* molecular dynamics simulations on

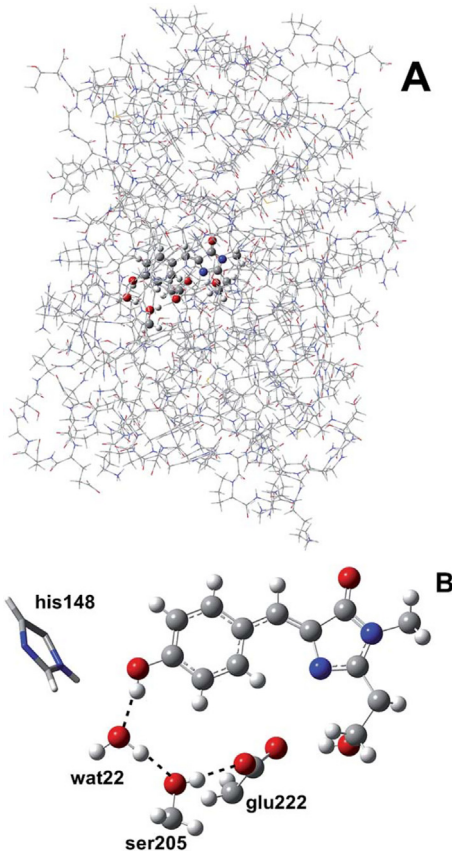

FIG. 9. (a) Schematic representation of GFP highlighting the ONIOM partition scheme: the chromophore completed by Ser65 side chain and the residues involved in the ESPT reaction (a crystallographic water molecule, Ser205 and Glu222) are shown in ball and stick representation, while the rest of the protein is shown with line representation. (b) Ball and stick representation of the chromophore and the residues involved in the hydrogen bond network and in the ESPT reaction. The His148 residue, hydrogen bonding the chromophore but not participating to the proton transfer, is also shown in tube representation since it is described at MM theory level. Adapted from Donati *et al.*, Chem. Sci. **9**, 1126–1135 (2018). Copyright 2018 The Royal Society of Chemistry.

GFP models also including the protein environment still lacked the photo-induced structural relaxation.[188,196,197] In another computational study, calculated intrinsic reaction coordinate on a reduced GFP model did include the rearrangement of the chromophore pocket, while not taking into account the full protein environment, causing in this way a limited exploration of the potential energy surface accessible to the system.[198]

The necessity of a computational strategy able to retain the entire protein environment while simulating the ESPT has driven toward the formulation of a novel protocol based on a AIMD where both the ground and excited electronic states are accurately simulated.[48]

2. A novel computational strategy to simulate the GFP excited state

The whole protein environment simulation represents the first requirement to simulate the ESPT. Of course, given the large number of degrees of freedom, the system is treated at different theory levels. More in detail, the entire hydrogen bond network including the chromophore, the crystallographic water molecule, Ser205 and Glu222, is treated at QM theory level based on a DFT approach in its time-independent or time-dependent formalism for either the ground or excited electronic state, respectively,[199–201] while the rest of the protein is modeled according to a molecular mechanics level. The ONIOM partition scheme[110–113] can be employed to handle this hybrid QM/MM description (a schematic picture is given in Fig. 9). First of all, a ground electronic state characterization is performed to calculate a minimum energy structure. A minimum energy structure can be considered representative as starting point for the AIMD simulations in the Born–Oppenheimer approximation[202,203] in both the singlet ground and excited electronic states. Indeed, because the main interest is to simulate the ESPT taking place at ultrafast timescale, a single potential energy surface treatment could be safely considered. A more complete description of GFP photophysics would have required accounting for non-adiabatic processes,[204] affecting the GFP dynamics at longer times. Unfortunately, this would not be possible for the ONIOM energy potential employed in this work.

Concerning the ground state, as can be observed from Fig. 10, the well-defined distributions of some key structural quantities involving intermolecular oxygen distances of the chromophore and residues involved in the hydrogen bond network, inter- and intramolecular oxygen–hydrogen distances, clearly reveal a tight well-defined stable hydrogen bond network where no evidence of rearrangement of the residues or of the HBDI conformation is found, confirming the fact that in the ground state the proton transfer seems not to be favored and also revealing that in the simulated timescale no pocket rearrangement takes place and so that starting configurations taken from the ground-state dynamics can be considered representative of the Franck–Condon region. Also, the chromophore N–C–C–C dihedral angle suggests a very low relative degree of freedom between the two rings, which enforces the picture of a well-defined hydrogen bond network and a HBDI substantially fixed in the protein pocket. Regarding the dihedral angle formed by the oxygens involved in the hydrogen bond network (OTyr-OWat-OSer205-OGlu222), a spread distribution is observed with values almost focused around 2.5 even though other populated regions appear in the 20–10 and the 20–40 intervals. Of course, a wider distribution is found in comparison with the previous one; however, it is expected given the fact that it is an intermolecular parameter also involving a water molecule that is more mobile with respect to the other residues.

Regarding the description of the electronic excited state, the TD-DFT was employed. From the ground-state AIMD simulation (7 ps long), four randomly chosen starting coordinates and related velocities were employed as starting points for the excited-state AIMD simulations. All these starting points are representative of the Franck–Condon region of the PES, while the choice to follow the non-equilibrium dynamics starting from different initial conditions allowed to check that the same ESPT mechanism was observed in the different cases. One of these initial structures was close to the minimum energy in terms of both chromophore conformation and its pocket arrangement.

A completely different scenario is found for the excited state. All the collected trajectories show a concerted ESPT mechanism where the proton transfer takes place from the HBDI to the crystallographic water molecule that in turn transfers the proton to Ser205, while

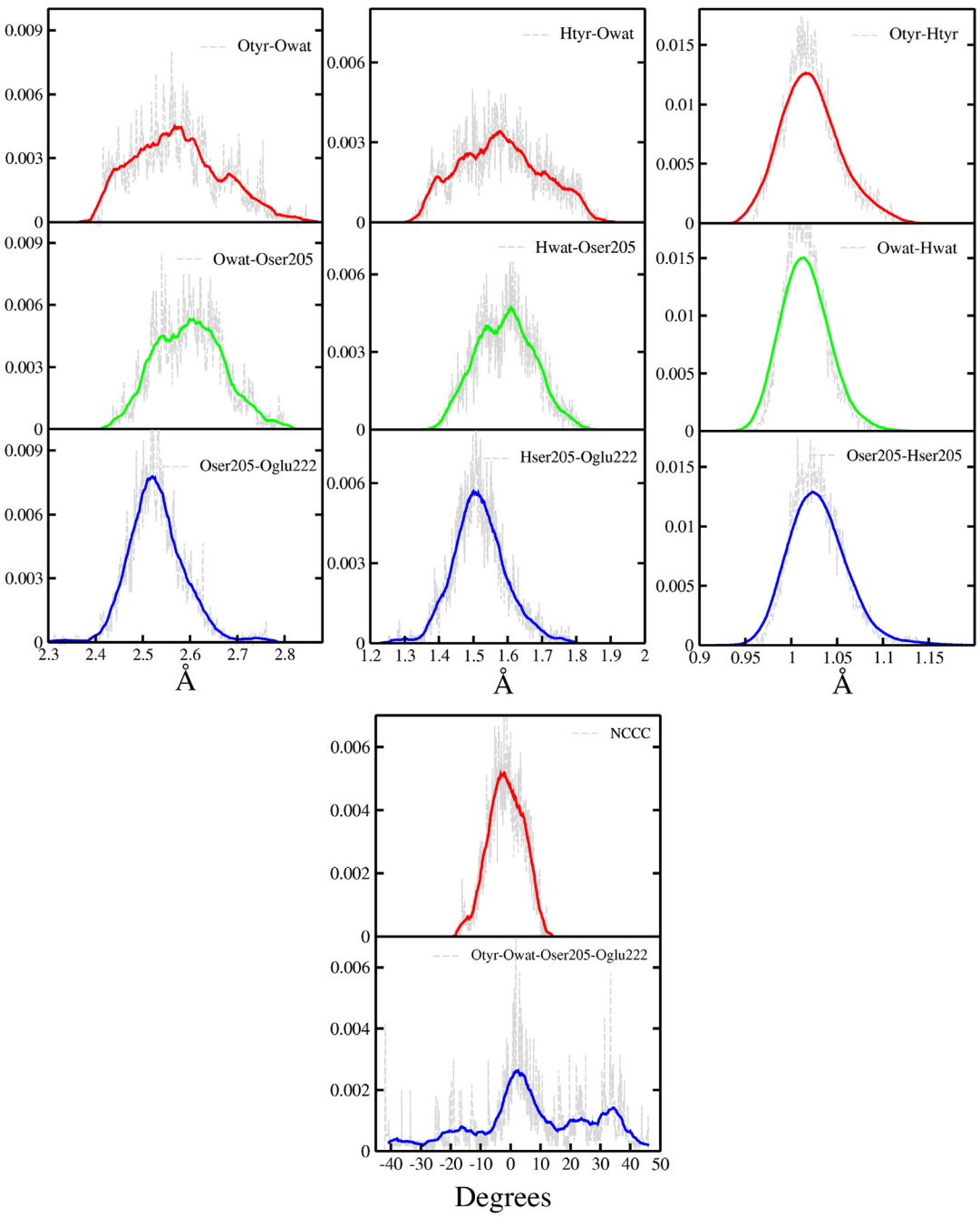

FIG. 10. Distances (Å) and dihedral angle (°) time-averaged distributions of the GFP PT network from the S0 AIMD simulation. Oxygen–oxygen, hydrogen–acceptor oxygen, and hydrogen–donor oxygen distances are shown in the top left, top middle, and top right columns, respectively. The chromophore N–C–C–C and the Otyr-Owat-Oser-Oglu dihedral angles are shown in the bottom columns. Average values are calculated every 100 points for the Otyr-Owat-Oser-Oglu case and every 50 points in all the other cases, and are shown with colored curves. Adapted from Donati *et al.*, Chem. Sci. **9**, 1126–1135 (2018). Copyright 2018 The Royal Society of Chemistry.

this one transfers its one to the final acceptor Glu222. The time evolution of the intermolecular oxygens and of the intra- and intermolecular oxygen–hydrogen distances is shown for one of the simulated trajectories in Fig. 11 where the ESPT event is clearly observed. The chromophore N–C–C–C dihedral angle explores a much wider range of values in comparison with the ground electronic state, suggesting that a chromophore ring relative orientation is necessary for allowing the ESPT event. Indeed, such large out-of-plane conformation is

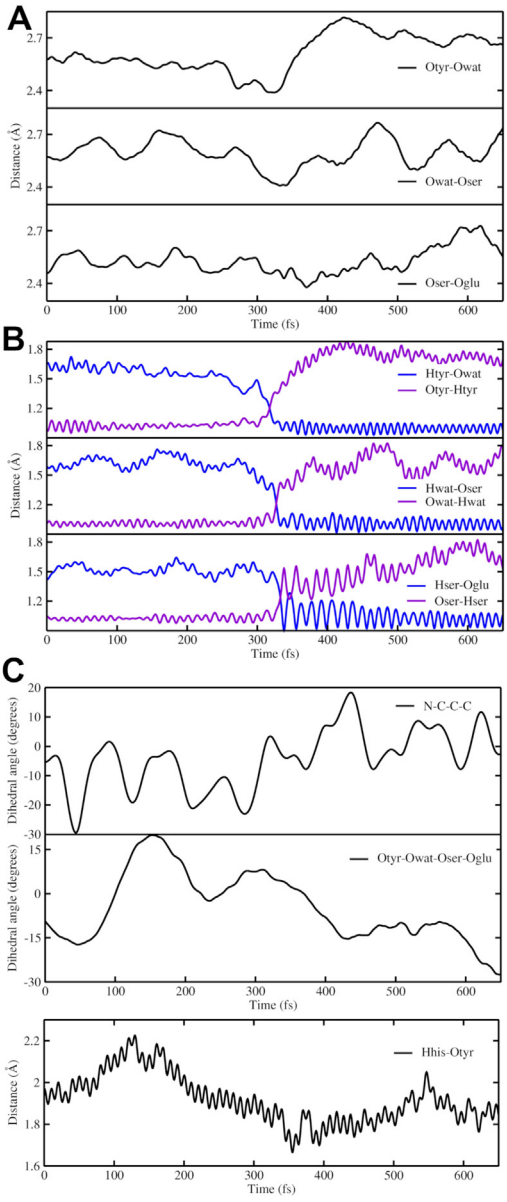

FIG. 11. Time evolution of the main intra- and intermolecular distances (Å) and dihedral angles (°) involved in the ESPT reaction from one of the S1 AIMD. (a) Intermolecular oxygen–oxygen distances: Otyr-Owat (top), Owat-OSer205 (middle), and OSer205-OGlu222 (bottom). (b) Hydrogen–donor oxygen (violet) and hydrogen–acceptor oxygen (blue) distances. From top to bottom panels: OTyr-HTyr and HTyr-Owat; Owat-Hwat and Hwat-OSer205; and OSer205-Hser205 and HSer205-OGlu222. (c) N–C–C–C chromophore dihedral angle (top panel), OTyr-Owat-OSer205-OGlu222 dihedral angle (middle), and HHis148-OTyr distance (bottom). Adapted from Donati *et al.*, Chem. Sci. **9**, 1126–1135 (2018). Copyright 2018 The Royal Society of Chemistry.

explored before the reaction takes place. The oxygen dihedral angle also explores large rearrangement, while it reaches values close to the planarity during the reaction suggesting that a coplanarity among the residues is necessary. Finally, the His148 approaches the oxygen of the HBDI phenolic ring, stabilizing the just formed anionic species. These peculiar structural arrangements are found in all the studied excited-state trajectories.

The convergence of results in terms of observed reaction mechanism and structural arrangements clearly demonstrates that the choice of the starting points for the excited-state AIMD simulations is taken correctly and that all these initial configurations are representative of the Franck–Condon region and can properly describe a non-equilibrium reaction event taking place on the ultrafast timescale. The choice of the initial conditions for an excited-state dynamics is challenging, especially for a system such as the GFP where the treatment of the entire protein is necessary.

E. Photo-induced metal to ligand charge transfer and the role of nuclear symmetry for a large and flexible metal complex in solution: Real-time electronic dynamics (EDs) initial sampling

Metal-to-ligand charge transfer (MLCT) states have a great importance for light-harvesting and photo-catalytic processes.[205–209] In particular, ruthenium-based polypyridyl complexes have proven quite efficient dye sensitizers for solar cells (DSSCs), when anchored onto nanocrystalline TiO_2 semiconductor thin films. The so-called $N3^{4-}$ Ru-complex $[Ru(dcbpy)_2(NCS)_2]^{4-}$, dcbpy = 4,4'-dicarboxy-2,2'-bipyridine (Fig. 12) represents in this regard a popular and widely studied example of this class of transition metal complexes.[208,210–219] The characterization of the ground state and equilibrium solvation of charge transfer systems such as $N3^{4-}$ represents therefore a first step toward the understanding of solvent effects in the ultrafast photo-induced CT dynamics and in time-resolved spectroscopic signals. N3 shows a complex dynamics involving multiple electronic states from the singlet ^{1}MLCT initially photo-induced ones toward a long-lived

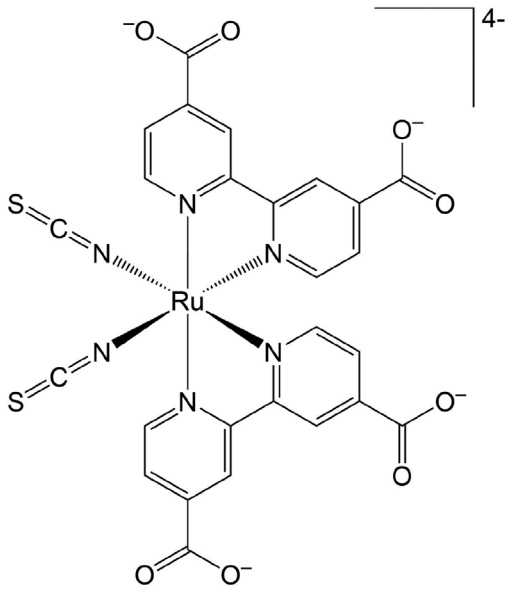

FIG. 12. Lewis structure of $[Ru(dcbpy)_2(NCS)_2]^{4-}$, dcbpy=(4,4′-dicarboxy-2,2′-bipyridine), or "$N3^{4-}$," a popular dye sensitizer for dye-sensitized solar cells.

final triplet ^{3}MLCT through inter-system crossing (ISC), both in solution[220–225] and on semiconductor substrates.[207,226–232] This suggests that each initially excited ^{1}MLCT state can potentially relax through a different pathway within the excited-state manifold.

We recently investigated the micro-solvation properties of $N3^{4-}$ in water solution through an *ab initio* molecular dynamics approach. In particular, an accurate modeling of solute–solvent interactions allowed us to describe environmental effects on $N3^{4-}$ coordination geometry and ligand vibrational modes.[81] A ground-state molecular dynamics trajectory of $N3^{4-}$ compound in explicit water solution was collected. A 22 Å radius spherical box was obtained from a previously equilibrated larger cubic box[233] with the experimental density at 298 K. This allowed us to explicitly include at least four solvation shells for each $N3^{4-}$ site and a total number of 1462 water molecules. The $N3^{4-}$ was placed at the center of the water spherical box and was treated at DFT quantum mechanical level, while the solvent molecules at an MM level. In particular, a flexible version of the TIP3P water model was employed, including an additional water bending term and able to describe coupled solute–solvent motions.[155] $N3^{4-}$ electronic structure was obtained using the global hybrid B3LYP density functional with the def2-SVP[234] basis set and associated electronic core potential (ECP) for Ru.[235] A hybrid QM/MM potential was constructed according to the ONIOM QM/MM scheme.[110,112,113,236] The electrostatic interaction between QM and MM layers was treated through an electronic embedding scheme, by the inclusion of the MM charges in the Hamiltonian of the QM portion. General AMBER force field[88] non-bonding parameters were assigned to the $N3^{4-}$ atoms. Finally, bulk effects were introduced combining NPBC and QM/MM AIMD.

$N3^{4-}$ solution structure appears distorted with respect to a symmetric C_2-like one. While the two N_{ax}-Ru-N_{eq} angles involving different dcbpy ligands, as well as the NCS-Ru-NCS angle, seem to keep their gas-phase values (Fig. 13 and Table IV), a deviation can be observed instead in the Ru-N(NCS)-C(NCS) angles, describing isothiocyanate coordination linearity. In fact, NCS^- coordination appears slightly bent in water solution ($\approx 177^\circ \pm 7^\circ$).

As revealed by solute–solvent $g(r)$ radial distribution functions, S(NCS^-) and O(dcbpy) sites strongly interact with the solvent, respectively, located at 3.10 and 2.70 Å (Fig. 14). On average, ∼3–4 water molecules are found in $N3^{4-}$ first solvation shells.

The dynamical deviation in water solution from the $N3^{4-}$ ideal C_2 symmetry was then investigated. In fact, finite temperature and solvation effects can instantaneously lower such symmetry to some extent. This, in turn, can allow to overcome in part symmetry-based

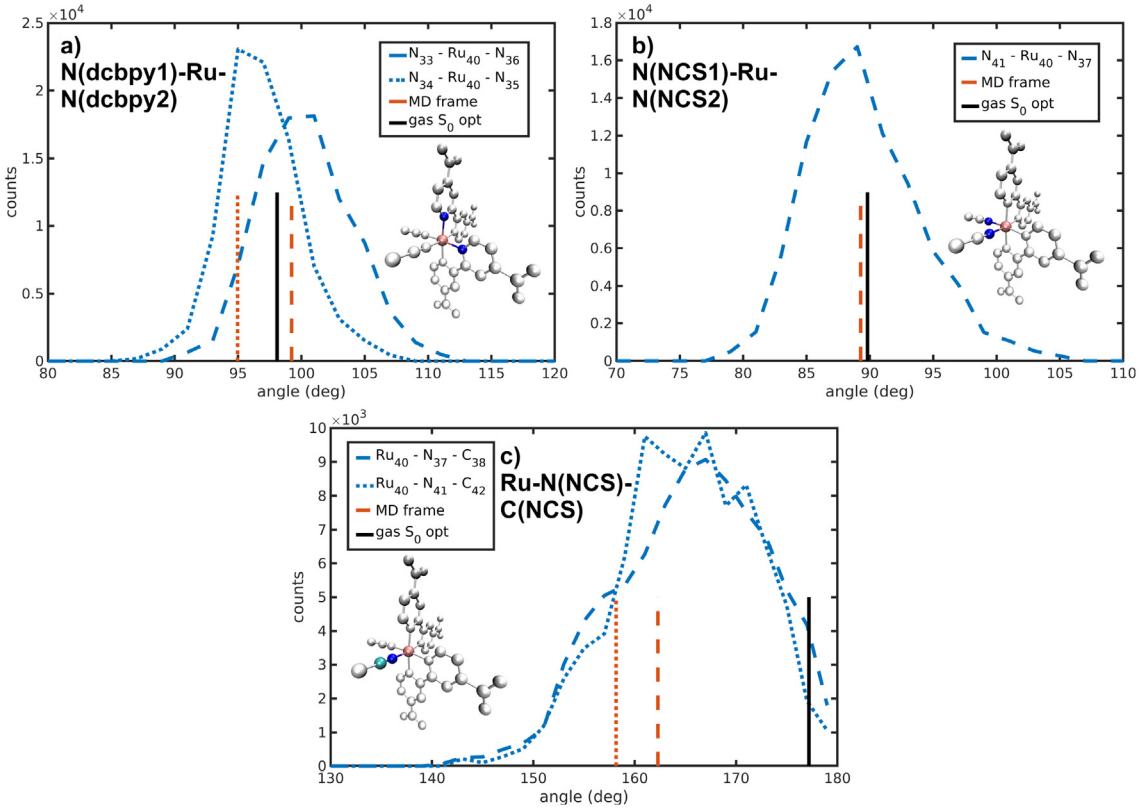

FIG. 13. Selected structural distributions from $N3^{4-}$ *ab initio* molecular dynamics in explicit water solution. The N(dcbpy1)-Ru-N(dcbpy2), N(NCS1)-Ru-N(NCS2), and Ru-N(NCS)-C(NCS) angles are reported. Please refer to the insets for the definition of these structural parameters. In particular, a distortion from linearity of the Ru-NCS coordination (∼165° Ru–N–C angle) with respect to the gas-phase optimized structure can be observed. The vertical black and red bars represent values from an optimized gas-phase structure and from the snapshot selected for future RT-TD-DFT electronic dynamics. Adapted with permission from Perrella *et al.*, Phys. Chem. Chem. Phys. **23**, 22885 (2021).[81] Copyright 2021 Royal Society of Chemistry.

TABLE IV. Mean (s.d.) $N3^{4-}$ structural parameters from AIMD trajectory in water solution. Values from $N3^{4-}$ in either vacuum or from a $N3^{4-}$ water cluster with implicit solvent (cluster) are also given for comparison. A single value is reported for the vacuum and cluster models due to symmetry. Values are in degrees.

	Dynamics	Vacuum	Cluster
N_{ax}(dcbpy1)-Ru-N_{eq}(dcbpy2)	100 (4)	98.08	97.25
	97 (3)		
N(NCS1)-Ru-N(NCS2)	89 (4)	89.82	90.40
Ru-N(NCS)-C(NCS)	165 (7)	177.20	177.94
	165 (7)		

selection rules, increasing the transition probability of otherwise dark electronic states, and can contribute to localize Ru-polypyridyl MLCT excited states, with the photoexcited electron on only one bipyridine ligand.[210,217,221,237–244] As already pointed out, the localization of CT excitations is potentially relevant for intramolecular, inter-ligand electron transfer (ILET) processes among bpy acceptor ligands.[221,243,244]

A continuous symmetry measure (CSM) of $N3^{4-}$ minimal deviation from C_2 symmetry was evaluated along the previously collected water solution AIMD trajectory. The index proposed in Refs. 245–247 quantitatively measures the deviation of a structure from its images generated through the symmetry operations of a given point group (C_2 group for $N3^{4-}$). In particular, a lower value in the [0, 1] range corresponds to a more symmetric structure. To improve computational efficiency, a reduced $N3^{4-}$ model (a smaller model with a maximum C_2 symmetry) was employed for C_2-CSM calculations. The water solution AIMD sampling shows that two small CSM values (∼0.1 and 0.2) are the most populated, but sometimes the system seems to acquire also higher symmetry distortions (∼0.45) (Fig. 15). Therefore, $N3^{4-}$ at room temperature in water solution actually slightly deviates, on average, from the C_2 symmetry, due to its vibrational motions and solvent environment fluctuations (mean C_2-CSM: 0.21 ± 0.12).

Moreover, solute–solvent interactions can alter the vibrational signals of the most solvated groups. Indeed, a MD-based vibrational analysis of $N3^{4-}$ in water solution predicted frequency red-shifts of some vibrational modes of both NCS^- and dcbpy ligands. Generalized normal modes (GNMs), able to retain both anharmonicity and solvation effects, were extracted from the $N3^{4-}$ ground-state trajectory.[145,248–250]

AIMD-derived vibrational frequencies (Table V) predict solvent-induced red-shifts with respect to gas-phase harmonic values exceeding 100 cm^{-1} (e.g., dcbpy carboxylate asymmetric stretching and NCS^- C = N stretching), also better explaining the experimental water solution data.[251] It is also worth noting that a harmonic vibrational analysis on a small $N3^{4-}$–water cluster in an implicit solvent model cannot always account for such red-shifts.

After an extensive characterization of ground-state properties, the ultrafast evolution of $N3^{4-}$ ^{1}MLCT electronic structure and the resulting ILET processes in water solution can be then explored

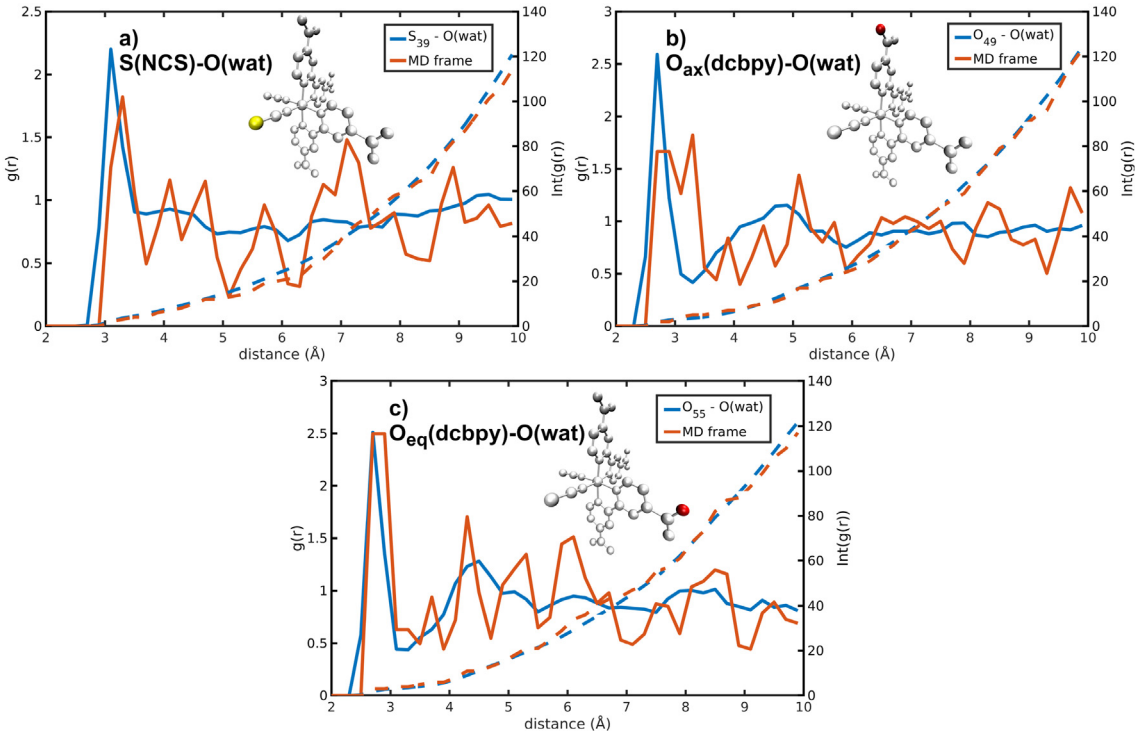

FIG. 14. Solute–solvent radial distribution functions from $N3^{4-}$ *ab initio* molecular dynamics in explicit water solution. Isothiocyanate sulfur and dcbpy carboxyl oxygen atoms appear highly solvated, as expected, interacting with 3–4 water molecules in the first solvation shell. RDFs from the frame selected for future RT-TD-DFT electronic dynamics are also reported. Adapted with permission from Perrella *et al.*, Phys. Chem. Chem. Phys. **23**, 22885 (2021).[81] Copyright 2021 Royal Society of Chemistry.

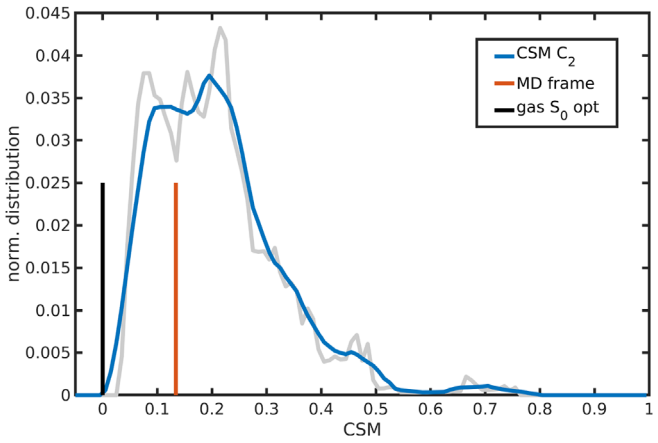

FIG. 15. Normalized distribution of the continuous symmetry measure (CSM) with respect to C_2 symmetry group sampled by $N3^{4-}$ AIMD in water solution. CSM has been calculated according to Ref. 245. A lower value in the [0, 1] range suggests a more symmetric structure. An averaged distribution function (blue curve) is shown for better clarity. The vertical black and red bars represent the zero value of the optimized gas-phase $N3^{4-}$ symmetric structure and that (0.13) of the AIMD-derived snapshot selected for future MLCT electronic dynamics. Adapted with permission from Perrella *et al.*, Phys. Chem. Chem. Phys. **23**, 22885 (2021).[81] Copyright 2021 Royal Society of Chemistry.

through excited-state electronic dynamics (ED), via real-time time-dependent DFT (RT-TD-DFT) approach.[162,252–257] Finite temperature and solvation effects have to be especially considered, since they may induce instantaneous symmetry-lowering from the ideal C_2 structure and so localization of the initial photoexcited electron. The excited states of interest are prepared by promoting an electron from a selected occupied molecular orbital to one that is unoccupied in the ground-state determinant ("Koopman excitation") according to the electronic transition of interest between the singlet ground state (S_0) and the n-th singlet excited state (S_n), resolved using a preliminary linear-response TD-DFT calculation. Excited-state electronic dynamics have to be performed on fixed nuclear configurations. Since our interest is focused on the ultrafast evolution of the electronic density after the photoexcitation (∼20 fs), electron–nuclear couplings are not expected to give a significant contribution in this time regime. Nevertheless, the choice of the nuclear geometry represents a quite critical step in the setup of a RT-TD-DFT simulation. In this regard, a snapshot was extracted from the $N3^{4-}$ water solution trajectory for future RT-TD-DFT simulations. This low-symmetry $N3^{4-}$ structure can account for vibrations and indirect solvent effects on ultrafast charge reorganization in the photo-induced CT states. Explicit solvation effects onto the excited-state electronic dynamics are added by explicitly including the surrounding water molecules. To mitigate over-polarization effects, the first-shell water molecules have to be treated at *ab initio* level and the other ones as embedded atomic charges.

TABLE V. Selected $N3^{4-}$ vibrational frequencies obtained through static harmonic and dynamical vibrational analysis. If available, also experimental, water solution, values[251] are reported for comparison.

		Static, harmonic		AIMD
	Experimental	Vacuum	Cluster	
ν_{symm}(COO) (cm^{-1})	1375	1368	1409	1354
ν_{asymm}(COO)	1596	1767	1700	1621
ν(CN)	2120	2210	2209	2080
ν(CS)		820	814	786

Although a single frame cannot of course be fully representative of the whole MD distribution, the snapshot selected for following MLCT electronic dynamics features relevant Ru(II) coordination structural parameters quite close to AIMD distribution maxima (Fig. 13), as well as solute–solvent radial distribution functions (and so the number of first-shell solvent molecules) comparable to those from the AIMD trajectory (Fig. 14). Moreover, the $N3^{4-}$ structure from this frame has, in contrast to the optimized gas phase one, a moderate symmetry distortion (0.13 C_2-CSM value, Fig. 15), belonging to the first highly populated peak at ∼0.1. Such structure can therefore account of the effects by slight symmetry deviations on the CT state ultrafast dynamics.

IV. CONCLUDING REMARKS AND OUTLOOK

Photo-induced non-equilibrium and relaxation dynamics require an explicit treatment of the electronic density, since computation protocols of light–matter interactions need to be capable of simultaneously describing the sudden electronic density reorganization and the subtle and time-dependent energetic balance in play with molecule/environment interactions. A reliable FES has to be based on high-level *ab initio* methods indeed, where hybrid density functionals represent a good compromise when proton transfers, non-covalent interactions, and hydrogen bond dynamics play important roles. The required accuracy cannot be easily achieved even via brute-force approaches, that is, including larger and larger explicit treatments of the systems at, that is, semi-empirical or even pure DFT levels, without gauging the quality of such molecule/environment interactions. Additionally, the collective environment motions have to be explicitly treated with flexible models, since these large amplitude vibrations often rule the (sub)picosecond relaxation dynamics. The case studies summarized in this review provided a strong validation of the potentials, the phase-space sampling, and initial condition choice, given the nice agreement with the experiments for what regards photophysical key features in complex environments, such as Stokes shift dynamics of a dye in water, the excited proton transfer reactivity of photo-acids in solution and in proteins, and finally the photo-induced charge transfer dynamics in non-covalent and metal–organic complexes in solution. In this review, we provide and extensive and detailed description on how DFT-based potentials are able to provide not only qualitative interpretations, but also a quantitative agreement with ultrafast time-resolved spectroscopies. In this regard, we described several case studies, spanning from the time-resolved fluorescence signal of MQ dye to the FSRS studies of pyranine, GFP, and 1-chloronaphthalene/tetracyanoethylene non-covalent charge transfer complex in solution.

Despite both the progress in more efficient and linear scaling algorithms and the employment of more powerful computer architectures and graphical processing units, we are convinced that hierarchical QM/MM/NPBC and efficient phase-sampling schemes are

recommended to achieve chemical accuracy in ultrafast time-resolved spectroscopy and photo-induced phenomena.

ACKNOWLEDGMENTS

G.D., F.P., and N.R. thank Gaussian Inc. for financial support. Italian Ministry of Education, University and Research (MIUR) is also gratefully acknowledged for financial support (A.P.: Project No. AIM1829571–1 CUP E61G19000090002, N.R.: Project Nos. PRIN 2017YJMPZN001 and PRIN 202082CE3T_002).

AUTHOR DECLARATIONS

Conflict of Interest

The authors have no conflicts to disclose.

DATA AVAILABILITY

All calculations were performed with a development version of the Gaussian software.[258] The data that support the findings of this study are available from the corresponding authors upon reasonable request.

REFERENCES

[1]K. E. Furse and S. A. Corcelli, "Molecular dynamics simulations of DNA solvation dynamics," J. Phys. Chem. Lett. **1**, 1813–1820 (2010).
[2]N. Nandi, K. Bhattacharyya, and B. Bagchi, "Dielectric relaxation and solvation dynamics of water in complex chemical and biological systems," Chem. Rev. **100**, 2013–2046 (2000).
[3]G. R. Fleming and M. Cho, "Chromophore-solvent dynamics," Annu. Rev. Phys. Chem. **47**, 109–134 (1996).
[4]J. W. Snyder, B. S. Fales, E. G. Hohenstein, B. G. Levine, and T. J. Martínez, "A direct-compatible formulation of the coupled perturbed complete active space self-consistent field equations on graphical processing units," J. Chem. Phys. **146**, 174113 (2017).
[5]O. Demel, J. Pittner, and F. Neese, "A local pair natural orbital-based multireference Mukherjee's coupled cluster method," J. Chem. Theory Comput. **11**, 3104–3114 (2015).
[6]C. Riplinger, B. Sandhoefer, A. Hansen, and F. Neese, "Natural triple excitations in local coupled cluster calculations with pair natural orbitals," J. Chem. Phys. **139**, 134101 (2013).
[7]R. E. Merrifield, "Ionized states in a one-dimensional molecular crystal," J. Chem. Phys. **34**, 1835–1839 (1961).
[8]W. Popp, D. Brey, R. Binder, and I. Burghardt, "Quantum dynamics of exciton transport and dissociation in multichromophoric systems," Annu. Rev. Phys. Chem. **72**, 591–616 (2021).
[9]P. O. Dral, X. Wu, L. Spörkel, A. Koslowski, W. Weber, R. Steiger, M. Scholten, and W. Thiel, "Semiempirical quantum-chemical orthogonalization-corrected methods: Theory, implementation, and parameters," J. Chem. Theory Comput. **12**, 1082–1096 (2016).
[10]W. Thiel, "Semiempirical quantum-chemical methods," Wiley Interdiscip. Rev. Comput. Mol. Sci. **4**, 145–157 (2014).
[11]C. Bannwarth, E. Caldeweyher, S. Ehlert, A. Hansen, P. Pracht, J. Seibert, S. Spicher, and S. Grimme, "Extended tight-binding quantum chemistry methods," Wiley Interdiscip. Rev. Comput. Mol. Sci. **11**, e1493 (2021).
[12]T. Cusati, G. Granucci, and M. Persico, "Photodynamics and time-resolved fluorescence of azobenzene in solution: A mixed quantum-classical simulation," J. Am. Chem. Soc. **133**, 5109–5123 (2011).
[13]E. Tapavicza, I. Tavernelli, and U. Rothlisberger, "Trajectory surface hopping within linear response time-dependent density-functional theory," Phys. Rev. Lett. **98**, 023001 (2007).
[14]A. Boziki, P. Baudin, E. Liberatore, N. Ashari Astani, and U. Rothlisberger, "A theoretical perspective of the ultrafast transient absorption dynamics of cspbbr3," J. Comput. Chem. **43**, 577–582 (2022).
[15]M. I. Dar, G. Jacopin, S. Meloni, A. Mattoni, N. Arora, A. Boziki, S. M. Zakeeruddin, U. Rothlisberger, and M. Grätzel, "Origin of unusual bandgap shift and dual emission in organic-inorganic lead halide perovskites," Sci. Adv. **2**, e1601156 (2016).
[16]M. Persico and G. Granucci, "An overview of nonadiabatic dynamics simulations methods, with focus on the direct approach versus the fitting of potential energy surfaces," Theor. Chem. Acc. **133**, 1526 (2014).
[17]P. Baudin, F. Mouvet, and U. Rothlisberger, "A multiple time step algorithm for trajectory surface hopping simulations," J. Chem. Phys. **156**, 034107 (2022).
[18]C. Adamo, M. Cossi, N. Rega, and V. Barone, "New computational strategies for the quantum mechanical study of biological systems in condensed phases," in *Theoretical Biochemistry, Theoretical and Computational Chemistry*, edited by L. A. Eriksson (Elsevier, Amsterdam, The Netherlands, 2001), Vol. 9, Chap. 12, pp. 467–538.
[19]V. Barone, R. Improta, and N. Rega, "Quantum mechanical computations and spectroscopy: From small rigid molecules in the gas phase to large flexible molecules in solution," Acc. Chem. Res. **41**, 605–616 (2008).
[20]C. Reichardt, "Solvatochromic dyes as solvent polarity indicators," Chem. Rev. **94**, 2319–2358 (1994).
[21]E. Krystkowiak, K. Dobek, and A. Maciejewski, "Origin of the strong effect of protic solvents on the emission spectra, quantum yield of fluorescence and fluorescence lifetime of 4-aminophthalimide: Role of hydrogen bonds in deactivation of s1-4-aminophthalimide," J. Photochem. Photobiol. **184**, 250–264 (2006).
[22]K. M. Solntsev, D. Huppert, and N. Agmon, "Photochemistry of superphotoacids. solvent effects," J. Phys. Chem. A **103**, 6984–6997 (1999).
[23]K. M. Solntsev, D. Huppert, L. M. Tolbert, and N. Agmon, "Solvatochromic shifts of super photoacids," J. Am. Chem. Soc. **120**, 7981–7982 (1998).
[24]H. A. Frank, J. A. Bautista, J. Josue, Z. Pendon, R. G. Hiller, F. P. Sharples, D. Gosztola, and M. R. Wasielewski, "Effect of the solvent environment on the spectroscopic properties and dynamics of the lowest excited states of carotenoids," J. Phys. Chem. B **104**, 4569–4577 (2000).
[25]V. Barone, N. Rega, T. Bally, and G. N. Sastry, "Ring-opening reaction of cyclobutene radical cation: Effect of solvent on competing pathways," J. Phys. Chem. A **103**, 217–219 (1999).
[26]R. Improta, N. Rega, C. Aleman, and V. Barone, "Conformational behavior of macromolecules in solution. homopolypeptides of α-aminoisobutyric acid as test cases," Macromolecules **34**, 7550–7557 (2001).
[27]E. Langella, N. Rega, R. Improta, O. Crescenzi, and V. Barone, "Conformational analysis of the tyrosine dipeptide analogue in the gas phase and in aqueous solution by a density functional/continuum solvent model," J. Comput. Chem. **23**, 650–661 (2002).
[28]A. Petrone, P. Caruso, S. Tenuta, and N. Rega, "On the optical absorption of the anionic GFP chromophore in vacuum, solution, and protein," Phys. Chem. Chem. Phys. **15**, 20536–20544 (2013).
[29]A. Petrone, J. Cerezo, F. J. A. Ferrer, G. Donati, R. Improta, N. Rega, and F. Santoro, "Absorption and emission spectral shapes of a prototype dye in water by combining classical/dynamical and quantum/static approaches," J. Phys. Chem. A **119**, 5426–5438 (2015).
[30]J. Cerezo, F. J. Avila Ferrer, G. Prampolini, and F. Santoro, "Modeling solvent broadening on the vibronic spectra of a series of coumarin dyes. From implicit to explicit solvent models," J. Chem. Theory Comput. **11**, 5810–5825 (2015).
[31]J. Cerezo, A. Petrone, F. J. A. Ferrer, G. Donati, F. Santoro, R. Improta, and N. Rega, "Electronic spectroscopy of a solvatochromic dye in water: Comparison of static cluster/implicit and dynamical/explicit solvent models on structures and energies," Theor. Chem. Acc. **135**, 263 (2016).
[32]J. Cerezo, G. Mazzeo, G. Longhi, S. Abbate, and F. Santoro, "Quantum-classical calculation of vibronic spectra along a reaction path: The case of the ECD of easily interconvertible conformers with opposite chiral responses," J. Phys. Chem. Lett. **7**, 4891–4897 (2016).
[33]D. Padula, J. Cerezo, G. Pescitelli, and F. Santoro, "The shape of the electronic circular dichroism spectrum of (2,6-dimethylphenyl)(phenyl)methanol: Interplay between conformational equilibria and vibronic effects," Phys. Chem. Chem. Phys. **19**, 32349–32360 (2017).

[34]J. Cerezo, D. Aranda, F. J. Avila Ferrer, G. Prampolini, G. Mazzeo, G. Longhi, S. Abbate, and F. Santoro, "Toward a general mixed quantum/classical method for the calculation of the vibronic ECD of a flexible dye molecule with different stable conformers: Revisiting the case of 2,2,2-trifluoro-anthrylethanol," Chirality **30**, 730–743 (2018).
[35]Y. Liu, J. Cerezo, N. Lin, X. Zhao, R. Improta, and F. Santoro, "Comparison of the results of a mean-field mixed quantum/classical method with full quantum predictions for nonadiabatic dynamics: Application to the $\pi\pi^*/n\pi^*$ decay of thymine," Theor. Chem. Acc. **137**, 40 (2018).
[36]M. J. Field, P. A. Bash, and M. Karplus, "A combined quantum mechanical and molecular mechanical potential for molecular dynamics simulations," J. Comput. Chem. **11**, 700–733 (1990).
[37]W. Yang, R. Bitetti-Putzer, and M. Karplus, "Chaperoned alchemical free energy simulations: A general method for QM, MM, and QM/MM potentials," J. Chem. Phys. **120**, 9450–9453 (2004).
[38]Q. Cui and M. Karplus, "Triosephosphate isomerase: A theoretical comparison of alternative pathways," J. Am. Chem. Soc. **123**, 2284–2290 (2001).
[39]Q. Cui and M. Karplus, "Quantum mechanics/molecular mechanics studies of triosephosphate isomerase-catalyzed reactions: Effect of geometry and tunneling on proton-transfer rate constants," J. Am. Chem. Soc. **124**, 3093–3124 (2002).
[40]J. Gao, S. Ma, D. T. Major, K. Nam, J. Pu, and D. G. Truhlar, "Mechanisms and free energies of enzymatic reactions," Chem. Rev. **106**, 3188–3209 (2006).
[41]K.-Y. Wong and J. Gao, "The reaction mechanism of paraoxon hydrolysis by phosphotriesterase from combined QM/MM simulations," Biochemistry **46**, 13352–13369 (2007).
[42]H. Yin, H. Li, A. Grofe, and J. Gao, "Active-site heterogeneity of lactate dehydrogenase," ACS Catal. **9**, 4236–4246 (2019).
[43]D. Riccardi, P. Schaefer, Yang, H. Yu, N. Ghosh, X. Prat-Resina, P. König, G. Li, D. Xu, H. Guo, M. Elstner, and Q. Cui, "Development of effective quantum mechanical/molecular mechanical (QM/MM) methods for complex biological processes," J. Phys. Chem. B **110**, 6458–6469 (2006).
[44]V. Vaissier Welborn and T. Head-Gordon, "Computational design of synthetic enzymes," Chem. Rev. **119**, 6613–6630 (2019).
[45]A. V. Nemukhin and B. L. Grigorenko, "QM/MM approaches shed light on GFP puzzles," in *QM/MM Studies of Light-Responsive Biological Systems*, edited by T. Andruniów and M. Olivucci (Springer International Publishing, Cham, 2021), pp. 271–292.
[46]A. V. Nemukhin, B. L. Grigorenko, M. G. Khrenova, and A. I. Krylov, "Computational challenges in modeling of representative bioimaging proteins: GFP-like proteins, flavoproteins, and phytochromes," J. Phys. Chem. B **123**, 6133–6149 (2019).
[47]V. Bolnykh, J. M. H. Olsen, S. Meloni, M. P. Bircher, E. Ippoliti, P. Carloni, and U. Rothlisberger, "Extreme scalability of DFT-based QM/MM MD simulations using MiMiC," J. Chem. Theory Comput. **15**, 5601–5613 (2019).
[48]G. Donati, A. Petrone, P. Caruso, and N. Rega, "The mechanism of a green fluorescent protein proton shuttle unveiled in the time-resolved frequency domain by excited state *ab initio* dynamics," Chem. Sci. **9**, 1126–1135 (2018).
[49]D. Marx and J. Hutter, *Modern Methods and Algorithms of Quantum Chemistry* (John von Neumann Institute for Computing, Julic, Germany, 2000), Vol. 1, p. 301.
[50]C. L. Brooks III and M. Karplus, "Deformable stochastic boundaries in molecular dynamics," J. Chem. Phys. **79**, 6312–6325 (1983).
[51]M. Berkowitz, C. L. Brooks III, and S. A. Adelman, "Generalized langevin theory for many-body problems in chemical dynamics: Modelling of solid and liquid state response functions," J. Chem. Phys. **72**, 3889–3898 (1980).
[52]K. Kratky, "New boundary conditions for computer experiments of thermodynamic systems," J. Chem. Phys. **37**, 205–217 (1980).
[53]E.-S. Riihimäki, J. M. Martínez, and L. Kloo, "An evaluation of non-periodic boundary condition models in molecular dynamics simulations using prion octapeptides as probes," J. Mol. Struct. **760**, 91–98 (2006).
[54]D. Beglov and B. Roux, "Finite representation of an infinite bulk system: Solvent boundary potential for computer simulations," J. Chem. Phys. **100**, 9050–9063 (1994).
[55]N. Rega, G. Brancato, and V. Barone, "Non–periodic boundary conditions for *ab initio* molecular dynamics in condensed phase using localized basis functions," Chem. Phys. Lett. **422**, 367–371 (2006).
[56]G. Brancato, N. Rega, and V. Barone, "A quantum mechanical/molecular dynamics/mean field study of acrolein in aqueous solution: Analysis of H bonding and bulk effects on spectroscopic properties," J. Chem. Phys. **125**, 164515 (2006).
[57]G. Brancato, N. Rega, and V. Barone, "A hybrid explicit/implicit solvation method for first principle molecular dynamics simulations," J. Chem. Phys. **128**, 144501 (2008).
[58]N. Rega, G. Brancato, A. Petrone, P. Caruso, and V. Barone, "Vibrational analysis of x-ray absorption fine structure thermal factors by *ab initio* molecular dynamics: The Zn(II) ion in aqueous solution as a case study," J. Chem. Phys. **134**, 074504 (2011).
[59]N. Rega, S. S. Iyengar, G. A. Voth, H. B. Schlegel, T. Vreven, and M. J. Frisch, "Hybrid *ab-initio*/empirical molecular dynamics: Combining the ONIOM scheme with the atom-centered density matrix propagation (ADMP) approach," J. Phys. Chem. B **108**, 4210–4220 (2004).
[60]U. Raucci, F. Perrella, G. Donati, M. Zoppi, A. Petrone, and N. Rega, "*Ab-initio* molecular dynamics and hybrid explicit-implicit solvation model for aqueous and nonaqueous solvents: GFP chromophore in water and methanol solution as case study," J. Comput. Chem. **41**, 2228–2239 (2020).
[61]F. Coppola, F. Perrella, A. Petrone, G. Donati, and N. Rega, "A not obvious correlation between the structure of green fluorescent protein chromophore pocket and hydrogen bond dynamics: A choreography from *ab initio* molecular dynamics," Front. Mol. Biosci. **7**, 283 (2020).
[62]J. Hafner, C. Wolverton, and G. Ceder, "Toward computational materials design: The impact of density functional theory on materials research," MRS Bull. **31**, 659–668 (2006).
[63]J. Aarons, M. Sarwar, D. Thompsett, and C.-K. Skylaris, "Perspective: Methods for large-scale density functional calculations on metallic systems," J. Chem. Phys. **145**, 220901 (2016).
[64]R. Beaulac, Y. Feng, J. W. May, E. Badaeva, D. R. Gamelin, and X. Li, "Orbital pathways for mn^{2+}-carrier *sp–d* exchange in diluted magnetic semiconductor quantum dots," Phys. Rev. B **84**, 195324 (2011).
[65]P. J. Lestrange, P. D. Nguyen, and X. Li, "Calibration of energy-specific TDDFT for modeling K-edge XAS spectra of light elements," J. Chem. Theory Comput. **11**, 2994–2999 (2015).
[66]A. Petrone, J. J. Goings, and X. Li, "Quantum confinement effects on optical transitions in nanodiamonds containing nitrogen vacancies," Phys. Rev. B **94**, 165402 (2016).
[67]N. Li, Z. Zhu, C.-C. Chueh, H. Liu, B. Peng, A. Petrone, X. Li, L. Wang, and A. K.-Y. Jen, "Mixed cation $FA_XPEA_{1-x}PbI_3$ with enhanced phase and ambient stability toward high-performance perovskite solar cells," Adv. Energy Mater. **7**, 1601307 (2016).
[68]D. C. Gary, S. E. Flowers, W. Kaminsky, A. Petrone, X. Li, and B. M. Cossairt, "Single-crystal and electronic structure of a 1.3 nm indium phosphide nanocluster," J. Am. Chem. Soc. **138**, 1510–1513 (2016).
[69]G. Donati, D. B. Lingerfelt, C. M. Aikens, and X. Li, "Molecular vibration induced plasmon decay," J. Phys. Chem. C **121**, 15368–15374 (2017).
[70]S. Xu, J. E. T. Smith, S. Gozem, A. I. Krylov, and J. M. Weber, "Electronic spectra of tris-(2,2′-bipyridine)-M(ii) complex ions in vacuo (M = Fe and Os)," Inorg. Chem. **56**, 7029–7037 (2017).
[71]U. Raucci, M. G. Chiariello, F. Coppola, F. Perrella, M. Savarese, I. Ciofini, and N. Rega, "An electron density based analysis to establish the electronic adiabaticity of proton coupled electron transfer reactions," J. Comput. Chem. **41**, 1835–1841 (2020).
[72]F. Coppola, P. Cimino, U. Raucci, M. G. Chiariello, A. Petrone, and N. Rega, "Exploring the Franck–Condon region of a photoexcited charge transfer complex in solution to interpret femtosecond stimulated Raman spectroscopy: Excited state electronic structure methods to unveil non-radiative pathways," Chem. Sci. **12**, 8058–8072 (2021).
[73]M. G. Chiariello and N. Rega, "Exploring nuclear photorelaxation of pyranine in aqueous solution: An integrated *ab-initio* molecular dynamics and time resolved vibrational analysis approach," J. Phys. Chem. A **122**, 2884–2893 (2018).
[74]D. B. Lingerfelt, D. B. Williams-Young, A. Petrone, and X. Li, "Direct *ab initio* (meta-)surface-hopping dynamics," J. Chem. Theory Comput. **12**, 935–945 (2016).

[75]A. Petrone, D. B. Williams-Young, D. B. Lingerfelt, and X. Li, "*Ab initio* excited state transient Raman analysis," J. Phys. Chem. A **121**, 3958–3965 (2017).
[76]A. Wildman, G. Donati, F. Lipparini, B. Mennucci, and X. Li, "Nonequilibrium environment dynamics in a frequency-dependent polarizable embedding models," J. Chem. Theory Comput. **15**, 43–51 (2018).
[77]A. Petrone, D. B. Lingerfelt, D. B. Williams-Young, and X. Li, "*Ab initio* transient vibrational spectral analysis," J. Phys. Chem. Lett. **7**, 4501–4508 (2016).
[78]E. Battista, P. L. Scognamiglio, N. Di Luise, U. Raucci, G. Donati, N. Rega, P. A. Netti, and F. Causa, "Turn-on fluorescence detection of protein by molecularly imprinted hydrogels based on supramolecular assembly of peptide multi-functional blocks," J. Mater. Chem. B **6**, 1207–1215 (2018).
[79]F. Perrella, U. Raucci, M. G. Chiariello, M. Chino, O. Maglio, A. Lombardi, and N. Rega, "Unveiling the structure of a novel artificial heme-enzyme with peroxidase-like activity: A theoretical investigation," Biopolymers **109**, e23225 (2018).
[80]A. Petrone, G. Donati, P. Caruso, and N. Rega, "Understanding THz and IR signals beneath time-resolved fluorescence from excited-state *ab initio* dynamics," J. Am. Chem. Soc. **136**, 14866–14874 (2014).
[81]F. Perrella, A. Petrone, and N. Rega, "Direct observation of the solvent organization and nuclear vibrations of $[Ru(dcbpy)_2(NCS)_2]^{4-}$, [dcbpy = (4,4′-dicarboxy-2,2′-bipyridine)], *via ab initio* molecular dynamics," Phys. Chem. Chem. Phys. **23**, 22885–22896 (2021).
[82]G. Brancato, N. Rega, and V. Barone, "Molecular dynamics simulations in a *NpT ensemble* using non-periodic boundary conditions," Chem. Phys. Lett. **483**, 177–181 (2009).
[83]A. Y. Ben-Naim, *Solvation Thermodynamics* (Springer Science & Business Media, Boston, 2013).
[84]S. Miertuš, E. Scrocco, and J. Tomasi, "Electrostatic interaction of a solute with a continuum. a direct utilization of *ab initio* molecular potentials for the prevision of solvent effects," Chem. Phys. **55**, 117–129 (1981).
[85]B. Mennucci and J. Tomasi, "Continuum solvation models: A new approach to the problem of solute's charge distribution and cavity boundaries," J. Chem. Phys. **106**, 5151–5158 (1997).
[86]N. Rega, M. Cossi, and V. Barone, "Towards linear scaling in continuum solvent models: A new iterative procedure for energies and geometry optimizations," Chem. Phys. Lett. **293**, 221–229 (1998).
[87]G. Brancato, A. D. Nola, V. Barone, and A. Amadei, "A mean field approach for molecular simulations of fluid systems," J. Chem. Phys. **122**, 154109 (2005).
[88]J. Wang, R. Wolf, and J. Caldwell, "Development and testing of a general amber force field," J. Comput. Chem. **25**, 1157–1174 (2004).
[89]D. L. Bunker and W. L. Hase, "On non-RRKM unimolecular kinetics: Molecules in general, and CH_3NC in particular," J. Chem. Phys. **59**, 4621–4632 (1973).
[90]W. L. Hase, R. J. Wolf, and C. S. Sloane, "Trajectory studies of the molecular dynamics of ethyl radical decomposition," J. Chem. Phys. **71**, 2911–2928 (1979).
[91]R. J. Wolf and W. L. Hase, "Importance of angular momentum constraints in the product energy partitioning of model H-C-C- → H + C = C dissociation," J. Chem. Phys. **73**, 3010–3011 (1980).
[92]W. L. Hase and D. G. Buckowski, "Monte Carlo sampling of a microcanonical ensemble of classical harmonic oscillators," Chem. Phys. Lett. **74**, 284–287 (1980).
[93]S. Chapman and D. L. Bunker, "An exploratory study of reactant vibrational effects in CH_3+ H_2 and its isotopic variants," J. Chem. Phys. **62**, 2890–2899 (1975).
[94]C. S. Sloane and W. L. Hase, "On the dynamics of state selected unimolecular reactions: Chloroacetylene dissociation and predissociation," J. Chem. Phys. **66**, 1523–1533 (1977).
[95]W. L. Hase, D. M. Ludlow, R. J. Wolf, and T. Schlick, "Translational and vibrational energy dependence of the cross section for H + C_2H_4 $C_2H_5^*$," J. Phys. Chem. **85**, 958–968 (1981).
[96]D. L. Clarke and M. A. Collins, "A classical trajectory study of the high CH and CD overtones in benzene and perdeuterobenzene," J. Chem. Phys. **86**, 6871–6881 (1987).
[97]J. C. Light, "Statistical theory of bimolecular exchange reactions," Discuss. Faraday Soc. **44**, 14–29 (1967).
[98]A. F. Wagner and D. G. Truhlar, "Comment on enhancement of the reaction cross section of He+H_2^+ → HeH^+ + H by vibrational excitation of H_2^+ and the treatment of nuclear spin by the statistical phase-space theory," J. Chem. Phys. **57**, 4063–4064 (1972).
[99]D. G. Truhlar, "Enhancement of the reaction cross section of He + H_2^+ → HeH^+ + H by vibrational excitation of H_2^+ according to the statistical phase-space theory," J. Chem. Phys. **56**, 1481–1486 (1972).
[100]D. G. Truhlar, "Intermediate coupling probability matrix approach to chemical reactions. dependence of the reaction cross section for potassium + hydrochloric acid → potassium chloride + hydrogen on initial translational and vibrational energy," J. Am. Chem. Soc. **97**, 6310–6317 (1975).
[101]C. Rebick, R. D. Levine, and R. B. Bernstein, "Energy requirements and energy disposal: Reaction probability matrices and a computational study of a model system," J. Chem. Phys. **60**, 4977–4989 (1974).
[102]R. D. Levine and J. Manz, "The effect of reagent energy on chemical reaction rates: An information theoretic analysis," J. Chem. Phys. **63**, 4280–4303 (1975).
[103]H. Kaplan, R. Levine, and J. Manz, "The dependence of the reaction rate constant on reagent excitation: The implications of detailed balance," Chem. Phys. **12**, 447–461 (1976).
[104]E. Pollak and R. Levine, "The different roles of reagent vibrational excitation for endothermic and exothermic reactions," Chem. Phys. Lett. **39**, 199–204 (1976).
[105]C. F. Chapman, R. S. Fee, and M. Maroncelli, "Measurements of the solute dependence of solvation dynamics in 1-propanol: The role of specific hydrogen-bonding interactions," J. Phys. Chem. **99**, 4811–4819 (1995).
[106]M. Sajadi, T. Obernhuber, S. A. Kovalenko, M. Mosquera, B. Dick, and N. P. Ernsting, "Dynamic polar solvation is reported by fluorescing 4-aminophthalimide faithfully despite H-bonding," J. Phys. Chem. A **113**, 44–55 (2009).
[107]D. W. Anthon and J. H. Clark, "Picosecond excited-state solvation dynamics of 9,9′-bianthryl in alcohol solutions," J. Phys. Chem. **91**, 3530–3536 (1987).
[108]J. Yu and M. Berg, "Resorufin as a probe for the dynamics of solvation by hydrogen bonding," Chem. Phys. Lett. **208**, 315–320 (1993).
[109]A. J. Benigno, E. Ahmed, and M. Berg, "The influence of solvent dynamics on the lifetime of solute–solvent hydrogen bonds," J. Chem. Phys. **104**, 7382–7394 (1996).
[110]M. Svensson, S. Humbel, R. D. Froese, T. Matsubara, S. Sieber, and K. Morokuma, "ONIOM: A multilayered integrated MO + MM method for geometry optimizations and single point energy predictions. A test for Diels-Alder reactions and $Pt(P(t\text{-}Bu)_3)_2$ + H_2 oxidative addition," J. Phys. Chem. **100**, 19357–19363 (1996).
[111]T. Vreven and K. Morokuma, "Hybrid methods: ONIOM (QM:MM) and QM/MM," Annu. Rep. Comput. Chem. **2**, 35–51 (2006).
[112]T. Vreven, K. S. Byun, I. Komáromi, S. Dapprich, J. A. Montgomery, Jr., K. Morokuma, and M. J. Frisch, "Combining quantum mechanics methods with molecular mechanics methods in ONIOM," J. Chem. Theory Comput. **2**, 815–826 (2006).
[113]L. W. Chung, W. M. C. Sameera, R. Ramozzi, A. J. Page, M. Hatanaka, G. P. Petrova, T. V. Harris, X. Li, Z. Ke, F. Liu, H. Li, L. Ding, and K. Morokuma, "The ONIOM method and its applications," Chem. Rev. **115**(12), 5678–5796 (2015).
[114]A. D. Becke, "Density-functional thermochemistry. III. The role of exact exchange," J. Chem. Phys. **98**, 5648 (1993).
[115]A. D. Becke, "Density-functional exchange-energy approximation with correct asymptotic behavior," Phys. Rev. A **38**, 3098 (1988).
[116]C. Lee, W. Yang, and R. G. Parr, "Development of the Colle-Salvetti correlation-energy formula into a functional of the electron density," Phys. Rev. B **37**, 785 (1988).
[117]B. Miehlich, A. Savin, H. Stoll, and H. Preuss, "Results obtained with the correlation energy density functionals of Becke and Lee, Yang and Parr," Chem. Phys. Lett. **157**, 200–206 (1989).
[118]W. L. Jorgensen, J. Chandrasekhar, J. D. Madura, R. W. Impey, and M. L. Klein, "Comparison of simple potential functions for simulating liquid water," J. Chem. Phys. **79**, 926–935 (1983).

[119]H. B. Schlegel, J. M. Millam, S. S. Iyengar, G. A. Voth, A. D. Daniels, G. E. Scuseria, and M. J. Frisch, "*Ab initio* molecular dynamics: Propagating the density matrix with Gaussian orbitals," J. Chem. Phys. **114**, 9758–9763 (2001).
[120]S. S. Iyengar, H. B. Schlegel, J. M. Millam, G. A. Voth, G. E. Scuseria, and M. J. Frisch, "*Ab initio* molecular dynamics: Propagating the density matrix with Gaussian orbitals. II. Generalizations based on mass-weighting, idempotency, energy conservation and choice of initial conditions," J. Chem. Phys. **115**, 10291–10302 (2001).
[121]H. B. Schlegel, S. S. Iyengar, X. Li, J. M. Millam, G. A. Voth, G. E. Scuseria, and M. J. Frisch, "*Ab initio* molecular dynamics: Propagating the density matrix with Gaussian orbitals. III. Comparison with Born-Oppenheimer dynamics," J. Chem. Phys. **117**, 8694–8704 (2002).
[122]U. Raucci, M. G. Chiariello, and N. Rega, "Modeling excited-state proton transfer to solvent: A dynamics study of a super photoacid with a hybrid implicit/explicit solvent model," J. Chem. Theory Comput. **16**, 7033–7043 (2020).
[123]R. Simkovitch, N. Karton-Lifshin, S. Shomer, D. Shabat, and D. Huppert, "Ultrafast excited-state proton transfer to the solvent occurs on a hundred-femtosecond time-scale," J. Phys. Chem. A **117**, 3405 (2013).
[124]T. Yanai, D. P. Tew, and N. C. Handy, "A new hybrid exchange–correlation functional using the Coulomb-attenuating method (CAM-B3LYP)," Chem. Phys. Lett. **393**, 51–57 (2004).
[125]R. R. Frontiera and R. A. Mathies, "Femtosecond stimulated Raman spectroscopy," Laser Photonics Rev. **5**, 102–113 (2011).
[126]P. Kukura, D. W. McCamant, and R. A. Mathies, "Femtosecond stimulated Raman spectroscopy," Annu. Rev. Phys. Chem. **58**, 461–488 (2007).
[127]D. R. Dietze and R. A. Mathies, "Femtosecond stimulated Raman spectroscopy," ChemPhysChem **17**, 1224 (2016).
[128]H.-T. Chang, A. Guggenmos, C. T. Chen, J. Oh, R. Géneaux, Y.-D. Chuang, A. M. Schwartzberg, S. Aloni, D. M. Neumark, and S. R. Leone, "Coupled valence carrier and core-exciton dynamics in WS_2 probed by few-femtosecond extreme ultraviolet transient absorption spectroscopy," Phys. Rev. B **104**, 064309 (2021).
[129]H. J. Marroux, A. P. Fidler, A. Ghosh, Y. Kobayashi, K. Gokhberg, A. I. Kuleff, S. R. Leone, and D. M. Neumark, "Attosecond spectroscopy reveals alignment dependent core-hole dynamics in the ICL molecule," Nat. Commun. **11**, 5810 (2020).
[130]C. Fang, R. R. Frontiera, R. Tran, and R. A. Mathies, "Mapping GFP structure evolution during proton transfer with femtosecond Raman spectroscopy," Nature **462**, 200–204 (2009).
[131]Y. Wang, W. Liu, L. Tang, B. Oscar, F. Han, and C. Fang, "Early time excited-state structural evolution of pyranine in methanol revealed by femtosecond stimulated Raman spectroscopy," J. Phys. Chem. A **117**, 6024 (2013).
[132]P. Kukura, D. W. McCamant, S. Yoon, D. B. Wandschneider, and R. A. Mathies, "Structural observation of the primary isomerization in vision with femtosecond-stimulated Raman," Science **310**, 1006 (2005).
[133]G. A. Worth, H.-D. Meyer, H. Köppel, L. Cederbaum, and I. Burghardt, "Using the MCTDH wavepacket propagation method to describe multimode non-adiabatic dynamics," Int. Rev. Phys. Chem. **27**, 569–606 (2008).
[134]K. H. Hughes, C. D. Christ, and I. Burghardt, "Effective-mode representation of non-Markovian dynamics: A hierarchical approximation of the spectral density. I. Application to single surface dynamics," J. Chem. Phys. **131**, 024109 (2009).
[135]G. A. Worth and I. Burghardt, "Full quantum mechanical molecular dynamics using Gaussian wavepackets," Chem. Phys. Lett. **368**, 502–508 (2003).
[136]M. H. Beck, A. Jäckle, G. A. Worth, and H.-D. Meyer, "The multiconfiguration time-dependent Hartree (MCTDH) method: A highly efficient algorithm for propagating wavepackets," Phys. Rep. **324**, 1–105 (2000).
[137]P. Leiderman, L. Genosar, and D. Huppert, "Excited-state proton transfer: Indication of three steps in the dissociation and recombination process," J. Phys. Chem. A **109**, 5965 (2005).
[138]R. Simkovitch, S. Shomer, R. Gepshtein, and D. Huppert, "How fast can a proton-transfer reaction be beyond the solvent-control limit?," J. Phys. Chem. B **119**, 2253 (2015).
[139]D. Spry, A. Goun, and M. Fayer, "Deprotonation dynamics and Stokes shift of pyranine (HPTS)," J. Phys. Chem. A **111**, 230 (2007).
[140]W. Liu, Y. Wang, L. Tang, B. G. Oscar, L. Zhu, and C. Fang, "Panoramic portrait of primary molecular events preceding excited state proton transfer in water," Chem. Sci. **7**, 5484 (2016).
[141]W. Liu, F. Han, C. Smith, and C. Fang, "Ultrafast conformational dynamics of pyranine during excited state proton transfer in aqueous solution revealed by femtosecond stimulated Raman spectroscopy," J. Phys. Chem. B **116**, 10535 (2012).
[142]V. Barone, M. Biczysko, and J. Bloino, "Fully anharmonic IR and Raman spectra of medium-size molecular systems: Accuracy and interpretation," Phys. Chem. Chem. Phys. **16**, 1759 (2014).
[143]J. Bloino, A. Baiardi, and M. Biczysko, "Aiming at an accurate prediction of vibrational and electronic spectra for medium-to-large molecules: An overview," Int. J. Quantum Chem. **116**, 1543 (2016).
[144]M. G. Chiariello, U. Raucci, F. Coppola, and N. Rega, "Unveiling anharmonic coupling by means of excited state *ab initio* dynamics: Application to diarylethene photoreactivity," Phys. Chem. Chem. Phys. **21**, 3606–3614 (2019).
[145]N. Rega, "Vibrational analysis beyond the harmonic regime from *ab initio* molecular dynamics," Theor. Chem. Acc. **116**, 347–354 (2006).
[146]C. Torrence and G. P. Compo, "A practical guide to wavelet analysis," Bull. Am. Meteor. Soc. **79**, 61–78 (1998).
[147]H. Weng and K. Lau, "Wavelets, period doubling, and time-frequency localization with application to organization of convection over the tropical western pacific," J. Atmos. Sci. **51**, 2523 (1994).
[148]F. Muniz-Miranda, M. Pagliai, G. Cardini, and V. Schettino, "Wavelet transform for spectroscopic analysis: Application to diols in water," J. Chem. Theory Comput. **7**, 1109 (2011).
[149]I. Daubechies, "The wavelet transform, time-frequency localization and signal analysis," IEEE Trans. Inf. Theory **36**, 961 (1990).
[150]O. Rioul and M. Vetterli, "Wavelets and signal processing," IEEE Signal Process. Mag. **8**, 14 (1991).
[151]M. Farge, "Wavelet transforms and their applications to turbulence," Annu. Rev. Fluid Mech. **24**, 395 (1992).
[152]M. Cossi, N. Rega, G. Scalmani, and V. Barone, "Energies, structures, and electronic properties of molecules in solution with the C-PCM solvation model," J. Comput. Chem. **24**, 669–681 (2003).
[153]D. P. Hoffman, S. R. Ellis, and R. A. Mathies, "Characterization of a conical intersection in a charge-transfer dimer with two-dimensional time-resolved stimulated Raman spectroscopy," J. Phys. Chem. A **118**, 4955–4965 (2014).
[154]F. Han, W. Liu, and C. Fang, "Excited-state proton transfer of photoexcited pyranine in water observed by femtosecond stimulated Raman spectroscopy," Chem. Phys. **422**, 204 (2013).
[155]G. Donati, A. Petrone, and N. Rega, "Multiresolution continuous wavelet transform for studying coupled solute–solvent vibrations via *ab initio* molecular dynamics," Phys. Chem. Chem. Phys. **22**, 22645–22661 (2020).
[156]I. Garcia-Cuesta, A. M. Sánchez de Merás, and H. Koch, "Coupled cluster calculations of the vertical excitation energies of tetracyanoethylene," J. Chem. Phys. **118**, 8216–8222 (2003).
[157]J. C. Stires Iv, E. J. McLaurin, and C. P. Kubiak, "Infrared spectroscopic determination of the degree of charge transfer in complexes of TCNE with methyl-substituted benzenes," Chem. Commun. **2005**, 3532–3534.
[158]B. Milián, R. Pou-Amérigo, M. Merchán, and E. Ortí, "Theoretical study of the electronic excited states of tetracyanoethylene and its radical anion," Comp. Phys. Comm. **6**, 503–510 (2005).
[159]I. Rubtsov and K. Yoshihara, "Vibrational coherence in electron donor–acceptor complexes," J. Phys. Chem. A **103**, 10202–10212 (1999).
[160]S. R. Ellis, D. P. Hoffman, M. Park, and R. A. Mathies, "Difference bands in time-resolved femtosecond stimulated Raman spectra of photoexcited intermolecular electron transfer from chloronaphthalene to tetracyanoethylene," J. Phys. Chem. A **122**, 3594–3605 (2018).
[161]N. S. Kumar, M. D. Gujrati, and J. N. Wilson, "Evidence of preferential π-stacking: A study of intermolecular and intramolecular charge transfer complexes," Chem. Commun. **46**, 5464–5466 (2010).
[162]G. Donati, D. B. Lingerfelt, A. Petrone, N. Rega, and X. Li, "'Watching' polaron pair formation from first-principles electron-nuclear dynamics," J. Phys. Chem. A **120**, 7255–7261 (2016).
[163]M. G. Chiariello, G. Donati, and N. Rega, "Time-resolved vibrational analysis of excited state *ab initio* molecular dynamics to understand photorelaxation:

The case of the pyranine photoacid in aqueous solution," J. Chem. Theory Comput. **16**, 6007–6013 (2020).
[164]M. G. Chiariello, G. Donati, U. Raucci, F. Perrella, and N. Rega, "Structural origin and vibrational fingerprints of the ultrafast excited state proton transfer of the pyranine–acetate complex in aqueous solution," J. Phys. Chem. B **125**, 10273–10281 (2021).
[165]M. G. Chiariello, U. Raucci, G. Donati, and N. Rega, "Water-mediated excited state proton transfer of pyranine–acetate in aqueous solution: Vibrational fingerprints from *ab initio* molecular dynamics," J. Phys. Chem. A **125**, 3569–3578 (2021).
[166]S. S. Iyengar, H. B. Schlegel, G. A. Voth, J. M. Millam, G. E. Scuseria, and M. J. Frisch, "*Ab initio* molecular dynamics: Propagating the density matrix with Gaussian orbitals. IV. Formal analysis of the deviations from Born–Oppenheimer dynamics," Israel J. Chem. **42**, 191–202 (2002).
[167]H. B. Schlegel, "*Ab initio* molecular dynamics with Born–Oppenheimer and extended Lagrangian methods using atom centered basis functions," Bull. Korean Chem. Soc. **24**, 837–842 (2003).
[168]E. Glendening, A. Reed, and J. Carpenter, "NBO Version 3.1," J. Comput. Chem. **19**, 628 (1998).
[169]F. Weinhold, "Natural bond orbital analysis: A critical overview of relationships to alternative bonding perspectives," J. Comput. Chem. **33**, 2363–2379 (2012).
[170]A. E. Reed, L. A. Curtiss, and F. Weinhold, "Intermolecular interactions from a natural bond orbital, donor-acceptor viewpoint," Chem. Rev. **88**, 899–926 (1988).
[171]A. E. Reed, R. B. Weinstock, and F. Weinhold, "Natural population analysis," J. Chem. Phys. **83**, 735–746 (1985).
[172]S. J. Grabowski, "Non-covalent interactions—QTAIM and NBO analysis," J. Mol. Mod. **19**, 4713–4721 (2013).
[173]R. Send and F. Furche, "First-order nonadiabatic couplings from time-dependent hybrid density functional response theory: Consistent formalism, implementation, and performance," J. Chem. Phys. **132**, 044107 (2010).
[174]M. Chalfie, Y. Tu, G. Euskirchen, W. Ward, and D. C. Prasher, "Green fluorescent protein as a marker of gene expression," Biochem. Biophys. Res. Commun. **263**, 802 (1994).
[175]R. Y. Tsien, "The green fluorescent protein," Annu. Rev. Biochem. **67**, 509–544 (1998).
[176]M. Zimmer, "Green fluorescent protein (GFP): Applications, structure, and related photophysical behavior," Chem. Rev. **102**, 759 (2002).
[177]T. Kogure, S. Karasawa, T. Araki, K. Saito, M. Kinjo, and A. Miyawaki, "A fluorescent variant of a protein from the stony coral Montipora facilitates dual-color single-laser fluorescence cross-correlation spectroscopy," Nat. Biotechnol. **24**, 577 (2006).
[178]M. Matz, A. Fradkov, Y. Labas, A. Savitsky, A. Zaraisky, M. Markelov, and S. A. Lukyanov, "Fluorescent proteins from nonbioluminescent Anthozoa species," Nat. Biotechnol. **17**, 969 (1999).
[179]J. Kennis, I. van Stokkum, D. Peterson, A. Pandit, and R. Wachter, "Ultrafast proton shuttling in *Psammocora* cyan fluorescent protein," J. Phys. Chem. B **117**, 11134 (2013).
[180]M. Chattoraj, B. King, G. Bublitz, and S. Boxer, "Ultra-fast excited state dynamics in green fluorescent protein: Multiple states and proton transfer," Proc. Natl. Acad. Sci. **93**, 8362 (1996).
[181]K. Brejc, T. Sixma, P. Kitts, S. Kain, R. Tsien, M. Ormo, and S. Remington, "Structural basis for dual excitation and photoisomerization of the *Aequorea victoria* green fluorescent protein," Proc. Natl. Acad. Sci. **94**, 2306 (1997).
[182]D. Stoner-Ma, A. Jaye, P. Matousek, M. Towrie, and S. Meech, "Observation of excited-state proton transfer in green fluorescent protein using ultrafast vibrational spectroscopy," J. Am. Chem. Soc. **127**, 2864 (2005).
[183]J. J. Van Thor, G. Zanetti, K. Ronayne, and M. Towrie, "Structural events in the photocycle of green fluorescent protein," J. Phys. Chem. B **109**, 16099 (2005).
[184]D. Stoner-Ma, E. Melief, J. Nappa, K. Ronayne, P. Tonge, and S. Meech, "Proton relay reaction in green fluorescent protein (GFP): Polarization-resolved ultrafast vibrational spectroscopy of isotopically edited GFP," J. Phys. Chem. B **110**, 22009 (2006).
[185]M. D. Donato, L. van Wilderen, I. V. Stokkum, T. Stuart, J. Kennis, K. Hellingwerf, R. van Grondelle, and M. Groot, "Proton transfer events in GFP," Phys. Chem. Chem. Phys. **13**, 16295 (2011).
[186]M. Kondo, I. Heisler, D. Stoner-Ma, P. Tonge, and S. Meech, "Ultrafast proton transfer in the green fluorescent protein: Analysing the instantaneous emission at product state wavelengths," J. Photochem. Photobiol. A **234**, 21 (2012).
[187]J. J. Van Thor, C. Lincoln, B. Kellner, K. Bourdakos, L. Thompson, M. Bearpark, P. Champion, and J. Sage, "Ultrafast vibrational dynamics of parallel excited state proton transfer reactions in the green fluorescent protein," Vib. Spectrosc. **62**, 1 (2012).
[188]M. Nadal-Ferret, R. Gelabert, M. Moreno, and J. M. Lluch, "Transient low-barrier hydrogen bond in the photoactive state of green fluorescent protein," Phys. Chem. Chem. Phys. **17**, 30876 (2015).
[189]T. Fujisawa, H. Kuramochi, H. Hosoi, S. Takeuchi, and T. Tahara, "Role of coherent low-frequency motion in excited-state proton transfer of green fluorescent protein studied by time-resolved impulsive stimulated Raman spectroscopy," J. Am. Chem. Soc. **138**, 3942 (2016).
[190]B. Grigorenko, A. Nemukhin, I. Polyakov, D. Morozov, and A. Krylov, "First-principles characterization of the energy landscape and optical spectra of green fluorescent protein along the A → I → B proton transfer route," J. Am. Chem. Soc. **135**, 11541 (2013).
[191]B. Grigorenko, A. Krylov, and A. Nemukhin, "Molecular modeling clarifies the mechanism of chromophore maturation in the green fluorescent protein," J. Am. Chem. Soc. **139**, 10239–10249 (2017).
[192]D. Smyrnova, M. d. C. Marin, M. Olivucci, and A. Ceulemans, "On excited state reaction path in reversibly switchable fluorescent proteins," arXiv:1709.06911 (2017).
[193]R. Send, C. M. Suomivuori, V. R. Kaila, and D. Sundholm, "Coupled-cluster studies of extensive green fluorescent protein models using the reduced virtual space approach," J. Phys. Chem. B **119**, 2933–2945 (2015).
[194]M. T. BBeerepoot, A. H. Steindal, J. Kongsted, B. O. Brandsal, L. Frediani, K. Ruud, and M. H. Olsen, "A polarizable embedding DFT study of one-photon absorption in fluorescent proteins," Phys. Chem. Chem. Phys. **15**, 4735–4743 (2013).
[195]M. Wanko, P. Garcia-Risueno, and A. Rubio, "Excited states of the green fluorescent protein chromophore: Performance of *ab initio* and semi-empirical methods," Phys. Status Solidi B **249**, 392–400 (2012).
[196]O. Vendrell, R. Gelabert, M. Moreno, and J. Llunch, "Operation of the proton wire in green fluorescent protein. a quantum dynamics simulation," J. Phys. Chem. B **112**, 5500–5511 (2008).
[197]O. Vendrell, R. Gelabert, M. Moreno, and J. Llunch, "A potential energy function for heterogeneous proton-wires. ground and photoactive states of the proton-wire in the green fluorescent protein," J. Chem. Theory Comput. **4**, 1138 (2008).
[198]A. Petrone, P. Cimino, G. Donati, H. P. Hratchian, M. J. Frisch, and N. Rega, "On the driving force of the excited-state proton shuttle in the green fluorescent protein: A time-dependent density functional theory (TD-DFT) study of the intrinsic reaction path," J. Chem. Theory Comput. **12**, 4925–4933 (2016).
[199]M. E. Casida, C. Jamorski, K. C. Casida, and D. R. Salahub, "Molecular excitation energies to high-lying bound states from time-dependent density-functional response theory: Characterization and correction of the time-dependent local density approximation ionization threshold," J. Chem. Phys. **108**, 4439–4449 (1998).
[200]R. E. Stratmann, G. E. Scuseria, and M. J. Frisch, "An efficient implementation of time-dependent density-functional theory for the calculation of excitation energies of large molecules," J. Chem. Phys. **109**, 8218–8224 (1998).
[201]E. Runge and E. K. Gross, "Density-functional theory for time-dependent systems," Phys. Rev. Lett. **52**, 997–1000 (1984).
[202]K. Bolton, W. L. Hase, and G. H. Peslherbe, *Modern Methods for Multidimensional Dynamics Computation in Chemistry*, edited by D. L. Thompson (World Scientific, Singapore, 1998), Vol. 95, pp. 143–189.
[203]J. M. Millam, V. Bakken, W. Chen, W. L. Hase, and H. B. Schlegel, "*Ab initio* classical trajectories on the Born–Oppenheimer surface: Hessian-based integrators using fifth-order polynomial and rational function fits," J. Chem. Phys. **111**, 3800 (1999).
[204]G. Cui, Z. Lan, and W. Thiel, "Intramolecular hydrogen bonding plays a crucial role in the photophysics and photochemistry of the GFP chromophore," J. Am. Chem. Soc. **134**, 1662–1672 (2012).
[205]T. Mirkovic, E. E. Ostroumov, J. M. Anna, R. van Grondelle, Govindjee, and G. D. Scholes, "Light absorption and energy transfer in the antenna complexes of photosynthetic organisms," Chem. Rev. **117**, 249–293 (2017).

[206]A. Hagfeldt and M. Grätzel, "Molecular photovoltaics," Acc. Chem. Res. **33**, 269–277 (2000).
[207]N. A. Anderson and T. Lian, "Ultrafast electron transfer at the molecule-semiconductor nanoparticle interface," Annu. Rev. Phys. Chem. **56**, 491–519 (2005).
[208]M. Grätzel, "Solar energy conversion by dye-sensitized photovoltaic cells," Inorg. Chem. **44**, 6841–6851 (2005).
[209]S. Ardo and G. J. Meyer, "Photodriven heterogeneous charge transfer with transition-metal compounds anchored to TiO_2 semiconductor surfaces," Chem. Soc. Rev. **38**, 115–164 (2009).
[210]N. H. Damrauer, G. Cerullo, A. Yeh, T. R. Boussie, C. V. Shank, and J. K. McCusker, "Femtosecond dynamics of excited-state evolution in $[Ru(bpy)_3]^{2+}$," Science **275**, 54–57 (1997).
[211]J. K. McCusker and A. Vlček, "Ultrafast excited-state processes in inorganic systems," Acc. Chem. Res. **48**, 1207–1208 (2015).
[212]A. Hagfeldt, G. Boschloo, L. Sun, L. Kloo, and H. Pettersson, "Dye-sensitized solar cells," Chem. Rev. **110**, 6595–6663 (2010).
[213]B. Lee, J. He, R. P. Chang, and M. G. Kanatzidis, "All-solid-state dye-sensitized solar cells with high efficiency," Nature **485**, 486–489 (2012).
[214]M. Grätzel, "Dye-sensitized solar cells," J. Photochem. Photobiol. C **4**, 145–153 (2003).
[215]M. Chergui, "Ultrafast photophysics of transition metal complexes," Acc. Chem. Res. **48**, 801–808 (2015).
[216]E. A. Juban, A. L. Smeigh, J. E. Monat, and J. K. McCusker, "Ultrafast dynamics of ligand-field excited states," Coord. Chem. Rev. **250**, 1783–1791 (2006).
[217]J. K. McCusker, "Femtosecond absorption spectroscopy of transition metal charge-transfer complexes," Acc. Chem. Res. **36**, 876–887 (2003).
[218]M. K. Nazeeruddin, R. Humphry-Baker, P. Liska, and M. Grätzel, "Investigation of sensitizer adsorption and the influence of protons on current and voltage of a dye-sensitized nanocrystalline TiO_2 solar cell," J. Phys. Chem. B **107**, 8981–8987 (2003).
[219]Q.-B. Meng, K. Takahashi, X.-T. Zhang, I. Sutanto, T. Rao, O. Sato, A. Fujishima, H. Watanabe, T. Nakamori, and M. Uragami, "Fabrication of an efficient solid-state dye-sensitized solar cell," Langmuir **19**, 3572–3574 (2003).
[220]J. B. Asbury, R. J. Ellingson, H. N. Ghosh, S. Ferrere, A. J. Nozik, and T. Lian, "Femtosecond IR study of excited-state relaxation and electron-injection dynamics of $Ru(dcbpy)_2(NCS)_2$ in solution and on nanocrystalline TiO_2 and Al_2O_3 thin films," J. Phys. Chem. B **103**, 3110–3119 (1999).
[221]M. R. Waterland and D. F. Kelley, "Photophysics and relaxation dynamics of $Ru(4,4'$dicarboxy-$2,2'$-bipyridine$)_2$cis$(NCS)_2$ in solution," J. Phys. Chem. A **105**, 4019–4028 (2001).
[222]L. C. T. Shoute and G. R. Loppnow, "Excited-state metal-to-ligand charge transfer dynamics of a ruthenium(II) dye in solution and adsorbed on tio_2 nanoparticles from resonance Raman spectroscopy," J. Am. Chem. Soc. **125**, 15636–15646 (2003).
[223]B. E. Van Kuiken, N. Huse, H. Cho, M. L. Strader, M. S. Lynch, R. W. Schoenlein, and M. Khalil, "Probing the electronic structure of a photoexcited solar cell dye with transient x-ray absorption spectroscopy," J. Phys. Chem. Lett. **3**, 1695–1700 (2012).
[224]O. Bräm, F. Messina, A. M. El-Zohry, A. Cannizzo, and M. Chergui, "Polychromatic femtosecond fluorescence studies of metal-polypyridine complexes in solution," Chem. Phys. **393**, 51–57 (2012).
[225]R. Horvath, M. G. Fraser, C. A. Clark, X.-Z. Sun, M. W. George, and K. C. Gordon, "Nature of excited states of ruthenium-based solar cell dyes in solution: A comprehensive spectroscopic study," Inorg. Chem. **54**, 11697–11708 (2015).
[226]Y. Tachibana, J. E. Moser, M. Grätzel, D. R. Klug, and J. R. Durrant, "Subpicosecond interfacial charge separation in dye-sensitized nanocrystalline titanium dioxide films," J. Phys. Chem. **100**, 20056–20062 (1996).
[227]T. Hannappel, B. Burfeindt, W. Storck, and F. Willig, "Measurement of ultrafast photoinduced electron transfer from chemically anchored Ru-dye molecules into empty electronic states in a colloidal anatase TiO_2 film," J. Phys. Chem. B **101**, 6799–6802 (1997).
[228]J. R. Durrant, Y. Tachibana, I. Mercer, J. E. Moser, M. Grätzel, and D. R. Klug, "The excitation wavelength and solvent dependence of the kinetics of electron injection in $Ru(dcbpy)_2(NCS)_2$ sensitized nanocrystalline TiO_2 films," Z. Phys. Chem. **212**, 93–98 (1999).
[229]J. B. Asbury, E. Hao, Y. Wang, H. N. Ghosh, and T. Lian, "Ultrafast electron transfer dynamics from molecular adsorbates to semiconductor nanocrystalline thin films," J. Phys. Chem. B **105**, 4545–4557 (2001).
[230]J. Kallioinen, G. Benkö, V. Sundström, J. E. I. Korppi-Tommola, and A. P. Yartsev, "Electron transfer from the singlet and triplet excited states of $Ru(dcbpy)_2(NCS)_2$ into nanocrystalline TiO_2 thin films," J. Phys. Chem. B **106**, 4396–4404 (2002).
[231]J. B. Asbury, N. A. Anderson, E. Hao, X. Ai, and T. Lian, "Parameters affecting electron injection dynamics from ruthenium dyes to titanium dioxide nanocrystalline thin film," J. Phys. Chem. B **107**, 7376–7386 (2003).
[232]C. C. Rich, M. A. Mattson, and A. T. Krummel, "Direct measurement of the absolute orientation of N3 dye at gold and titanium dioxide surfaces with heterodyne-detected vibrational SFG spectroscopy," J. Phys. Chem. C **120**, 6601–6611 (2016).
[233]D. Case, H. Aktulga, K. Belfon, I. Ben-Shalom, S. Brozell, D. Cerutti, T. Cheatham III, V. Cruzeiro, T. Darden, R. Duke, G. Giambasu, M. Gilson, H. Gohlke, A. Goetz, R. Harris, S. Izadi, S. Izmailov, C. Jin, K. Kasavajhala, M. Kaymak, E. King, A. Kovalenko, T. Kurtzman, T. Lee, S. LeGrand, P. Li, C. Lin, J. Liu, T. Luchko, R. Luo, M. Machado, V. Man, M. Manathunga, K. Merz, Y. Miao, O. Mikhailovskii, G. Monard, H. Nguyen, K. O'Hearn, A. Onufriev, F. Pan, S. Pantano, R. Qi, A. Rahnamoun, D. Roe, A. Roitberg, C. Sagui, S. Schott-Verdugo, J. Shen, C. Simmerling, N. Skrynnikov, J. Smith, J. Swails, R. Walker, J. Wang, H. Wei, R. Wolf, X. Wu, Y. Xue, D. York, S. Zhao, and P. Kollman, Amber 2021.
[234]F. Weigend and R. Ahlrichs, "Balanced basis sets of split valence, triple zeta valence and quadruple zeta valence quality for H to Rn: Design and assessment of accuracy," Phys. Chem. Chem. Phys. **7**, 3297–3305 (2005).
[235]D. Andrae, U. Haeussermann, M. Dolg, H. Stoll, and H. Preuss, "Energy-adjusted *ab initio* pseudopotentials for the second and third row transition elements," Theor. Chem. Acc. **77**, 123–141 (1990).
[236]K. Morokuma, Q. Wang, and T. Vreven, "Performance evaluation of the three-layer ONIOM method: Case study for a zwitterionic peptide," J. Chem. Theory Comput. **2**, 1317–1324 (2006).
[237]K. Kalyanasundaram, "Photophysics, photochemistry and solar energy conversion with tris-(bipyridyl)ruthenium (II) and its analogues," Coord. Chem. Rev. **46**, 159–244 (1982).
[238]A. Juris, V. Balzani, F. Barigelletti, S. Campagna, P. l. Belser, and A. v. von Zelewsky, "Ru (II) polypyridine complexes: Photophysics, photochemistry, electrochemistry, and chemiluminescence," Coord. Chem. Rev. **84**, 85–277 (1988).
[239]E. M. Kober, B. P. Sullivan, and T. J. Meyer, "Solvent dependence of metal-to-ligand charge-transfer transitions. Evidence for initial electron localization in MLCT excited states of 2,2′-bipyridine complexes of ruthenium (II) and osmium (II)," Inorg. Chem. **23**, 2098–2104 (1984).
[240]R. F. Dallinger and W. H. Woodruff, "Time-resolved resonance Raman study of the lowest ($d\pi^*$, 3ct) excited state of tris-(2,2′-bipyridine)ruthenium (II)," J. Am. Chem. Soc. **101**, 4391–4393 (1979).
[241]D. H. Oh and S. G. Boxer, "Stark effect spectra of $Ru(diimine)_3^{2+}$ complexes," J. Am. Chem. Soc. **111**, 1130–1131 (1989).
[242]M. Myrick, R. Blakley, and M. DeArmond, "Time-resolved photoselection of $[Ru(bpy)_3]^{2+}$-exciton hopping in the excited state," J. Am. Chem. Soc. **109**, 2841–2842 (1987).
[243]B. P. Rimgard, J. Föhlinger, J. Petersson, M. Lundberg, B. Zietz, A. M. Woys, S. A. Miller, M. R. Wasielewski, and L. Hammarström, "Ultrafast interligand electron transfer in *cis*-$[Ru(4,4'$-dicarboxylate-$2,2'$-bipyridine$)_2(NCS)_2]^{4-}$ and implications for electron injection limitations in dye sensitized solar cells," Chem. Sci. **9**, 7958–7967 (2018).
[244]G. Benkö, J. Kallioinen, P. Myllyperkiö, F. Trif, J. E. Korppi-Tommola, A. P. Yartsev, and V. Sundström, "Interligand electron transfer determines triplet excited state electron injection in RuN3-sensitized TiO_2 films," J. Phys. Chem. B **108**, 2862–2867 (2004).
[245]M. Pinsky, C. Dryzun, D. Casanova, P. Alemany, and D. Avnir, "Analytical methods for calculating continuous symmetry measures and the chirality measure," J. Comput. Chem. **29**, 2712–2721 (2008).
[246]H. Zabrodsky, S. Peleg, and D. Avnir, "Continuous symmetry measures," J. Am. Chem. Soc. **114**, 7843–7851 (1992).

[247]M. Pinsky, D. Casanova, P. Alemany, S. Alvarez, D. Avnir, C. Dryzun, Z. Kizner, and A. Sterkin, "Symmetry operation measures," J. Comput. Chem. **29**, 190–197 (2008).
[248]A. Strachan, "Normal modes and frequencies from covariances in molecular dynamics or Monte Carlo simulations," J. Chem. Phys. **120**, 1–4 (2004).
[249]S. Thicoipe, P. Carbonniere, and C. Pouchan, "Comparison of static and dynamic methods of treatment of anharmonicity for the vibrational study of isolated and aqueous forms of guanine," Chem. Phys. Lett. **591**, 243–247 (2014).
[250]P. Carbonniere, A. Dargelos, I. Ciofini, C. Adamo, and C. Pouchan, "Vibrational analysis of glycine radical: A comparative *ab initio* static and dynamic study," Phys. Chem. Chem. Phys. **11**, 4375–4384 (2009).
[251]J. D. Gaynor, A. Petrone, X. Li, and M. Khalil, "Mapping vibronic couplings in a solar cell dye with polarization-selective two-dimensional electronic–vibrational spectroscopy," J. Phys. Chem. Lett. **9**, 6289–6295 (2018).
[252]C. T. Chapman, W. Liang, and X. Li, "Ultrafast coherent electron-hole separation dynamics in a fullerene derivative," J. Phys. Chem. Lett. **2**, 1189–1192 (2011).
[253]F. Ding, C. T. Chapman, W. Liang, and X. Li, "Mechanisms of bridge-mediated electron transfer: A TDDFT electronic dynamics study," J. Chem. Phys. **137**, 22A512 (2012).
[254]A. Petrone, D. B. Lingerfelt, N. Rega, and X. Li, "From charge-transfer to a charge-separated state: A perspective from the real-time TDDFT excitonic dynamics," Phys. Chem. Chem. Phys. **16**, 24457–24465 (2014).
[255]J. M. Kasper, P. J. Lestrange, T. F. Stetina, and X. Li, "Modeling $L_{2,3}$-edge x-ray absorption spectroscopy with real-time exact two-component relativistic time-dependent density functional theory," J. Chem. Theory Comput. **14**, 1998–2006 (2018).
[256]J. J. Goings, P. J. Lestrange, and X. Li, "Real-time time-dependent electronic structure theory," Wiley Interdiscip. Rev. Comput. Mol. Sci. **8**, e1341 (2018).
[257]X. Li, N. Govind, C. Isborn, A. E. DePrince, and K. Lopata, "Real-time time-dependent electronic structure theory," Chem. Rev. **120**, 9951–9993 (2020).
[258]M. J. Frisch, G. W. Trucks, H. B. Schlegel, G. E. Scuseria, M. A. Robb, J. R. Cheeseman, G. Scalmani, V. Barone, G. A. Petersson, H. Nakatsuji, X. Li, M. Caricato, A. V. Marenich, J. Bloino, B. G. Janesko, R. Gomperts, B. Mennucci, H. P. Hratchian, J. V. Ortiz, A. F. Izmaylov, J. L. Sonnenberg, D. Williams-Young, F. Ding, F. Lipparini, F. Egidi, J. Goings, B. Peng, A. Petrone, T. Henderson, D. Ranasinghe, V. G. Zakrzewski, J. Gao, N. Rega, G. Zheng, W. Liang, M. Hada, M. Ehara, K. Toyota, R. Fukuda, J. Hasegawa, M. Ishida, T. Nakajima, Y. Honda, O. Kitao, H. Nakai, T. Vreven, K. Throssell, J. A. Montgomery, Jr., J. E. Peralta, F. Ogliaro, M. J. Bearpark, J. J. Heyd, E. N. Brothers, K. N. Kudin, V. N. Staroverov, T. A. Keith, R. Kobayashi, J. Normand, K. Raghavachari, A. P. Rendell, J. C. Burant, S. S. Iyengar, J. Tomasi, M. Cossi, J. M. Millam, M. Klene, C. Adamo, R. Cammi, J. W. Ochterski, R. L. Martin, K. Morokuma, O. Farkas, J. B. Foresman, and D. J. Fox, *Gaussian 09 Developer Version H29P* (Gaussian Inc., Wallingford, CT, 2016).